Experimental and Theoretical Analysis of High Power Connectors for Hybrid Vehicles

by

Rujian Fu

A thesis submitted to the Graduate Faculty of
Auburn University
in partial fulfillment of the
requirements for the Degree of
Master of Science

Auburn, Alabama
May 9, 2011

Keywords: high power electric connector, fretting, vibration, finite element modeling

Approved by

Song-yul Choe, Chair, Associate Professor of Mechanical Engineering
Robert L. Jackson, Associate Professor of Mechanical Engineering
George T. Flowers, Professor of Mechanical Engineering

Abstract

Hybrid electric vehicles (HEV) are the next evolutionary step of the automobile which substantially increases fuel economy and reduces emissions. They are comprised of many new technologies so there is limited information on their overall life and reliability. The electrical connectors used in HEVs conduct much more power and are more susceptible to failure and reliability problems under the vibration, thermal cycling and humidity environment in a vehicle. This work presents a detailed study on the performance of a round pin, silver-plated high power connector used for hybrid vehicles, including experimental testing using a custom-designed test stand and theoretical analysis by finite element methods (FEM).

In order to emulate operational and environmental effects, a test stand is designed for the connector that is capable of measuring connector resistance, temperature and motions. When a connector is exposed to vibrations, experimental results show that the connector resistance increases and oscillates significantly. When the vibrations are stopped, connector resistance returns to a value that is close to the original state.

In order to analyze this phenomenon, a two-dimensional finite element model is developed to calculate relative displacement between the male part and female part of the connector. After being validated by experiments, the model shows that the simulated relative displacement is closely related to the changes of connector resistance under vibration, as measured in experiments. The relative displacement is then used as input for a three-dimensional finite element model that studies the time response of the contact spring. The simulation has

shown periodical contact gaps between the spring and other parts of the connector, which cause the changes in connector resistance during vibration.

Acknowledgments

I would like to express my deep appreciation to my advisor, Dr. Song-yul Choe, for giving me the opportunity to get involved in this research project. His wise suggestions and generous guidance assisted me to the fulfillment of my study. Without his valuable comments and detailed corrections to my papers and thesis, I would hardly finish my research program smoothly. I also would like to acknowledge to my committee member, Dr. Robert L. Jackson, for his continuous instructions and encouragement, which enabled me to develop a deep understanding in the research area. Special thanks would be given to another committee member, Dr. George T. Flowers, for his enlightening advice and great contribution of lab resources to the project. Finally, I would like to express my gratitude to my parents, Guangda Fu and Xiaoyan Li, for their unselfish support of my academic endeavor.

Table of Contents

List of Tables

List of Figures

List of Abbreviations

d	The relative displacement between male part and female part at the contact surfaces, equaling to $\|U_4 - U_1\|$ (unit: mm)
$F_{r,i}$	The contact force for the ith repeatable section of contact spring in radial direction, having two components in x direction ($F_{x,i}$) and y direction ($F_{y,i}$) (unit: N)
I_C	Current going through connector (A)
k_e	The equivalent spring constant of the simplified contact spring in two-dimensional finite element model (unit: N/mm)
M_i	The magnitude of the motion at certain position of the connector system (unit: mm)
R	Radius of male part of connector (unit: mm)
R_C	Connector resistance (unit: mΩ)
r_i	The radial displacement of the ith repeatable section of contact spring from steady state position (unit: mm)
T_C	Connector temperature (unit: ˚C)
U_0	The motion at the fixture, equal to $M_0 \angle \varphi_0$
U_1	The motion at female part, equal to $M_1 \angle \varphi_1$
U_2	The motion at the right end of male part, equal to $M_2 \angle \varphi_2$
U_3	The motion at the midpoint of cable, equal to $M_3 \angle \varphi_3$
U_4	The motion at the male part, equal to $M_4 \angle \varphi_4$

$\|U_2 - U_1\|$	The relative displacement between the right end of male part and female part
$\|U_4 - U_1\|$	The relative displacement between the male part and the female part at contact surfaces
V_C	Voltage drop of connector (unit: mV)
α_i	The angle from the direction of vibration to the radial direction of the i^{th} repeatable section of contact spring (unit: degree°)
ΔR_C	The temporary changes in connector resistance under vibration (unit: mΩ)
ΔT_C	The overall changes in connector temperature under vibration (unit: ˚C)
φ_i	The phase shift of the motion at certain position of the connector system (unit: degree°)

CHAPTER 1 INTRODUCTION

Hybrid electric vehicles (HEV) are the next evolutionary step of the automobile which substantially increases fuel economy and reduces emissions. However, the electrical systems which propel HEVs are fundamentally different from conventional technologies. There are technical barriers that prevent the success of hybrid electric propulsion systems. One of the crucial issues for hybrid systems is the reliability of electrical components, which should be guaranteed for the same period as the mechanical components.

High electrical power is required for new vehicles which use electrical propulsion. Typical hybrid systems use one or two electric motors that are mechanically connected to shafts and electrically to batteries via DC/AC inverters and DC/DC converter, as shown in Figure 1. Detachable power connectors are desired for durable and easily removed electrical connections. This is especially important for the easy replacement and repair of electrical components.

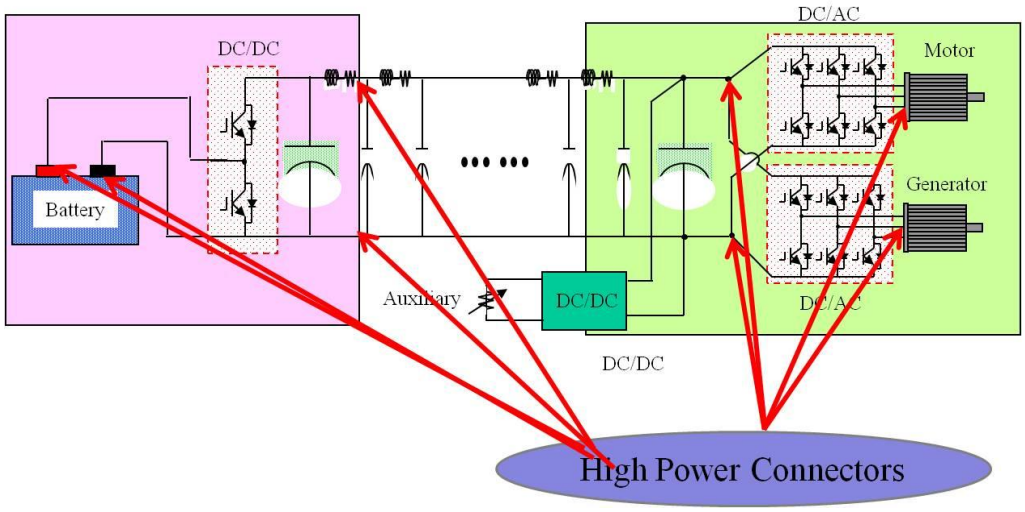

Figure 1: Electric systems for hybrid propulsion systems (from Dr. Song-yul Choe, unpublished)

HEV electrical connectors conduct much more power and are more susceptible to failure and reliability problems than the connectors in conventional vehicles. As shown in Figure 2, the power and voltage requirements for vehicles are steadily increasing as a vehicle transitions from a conventional vehicle to a mild hybrid all the way to a plug-in HEV. Therefore the connectors in these vehicles must be able to handle these higher powers.

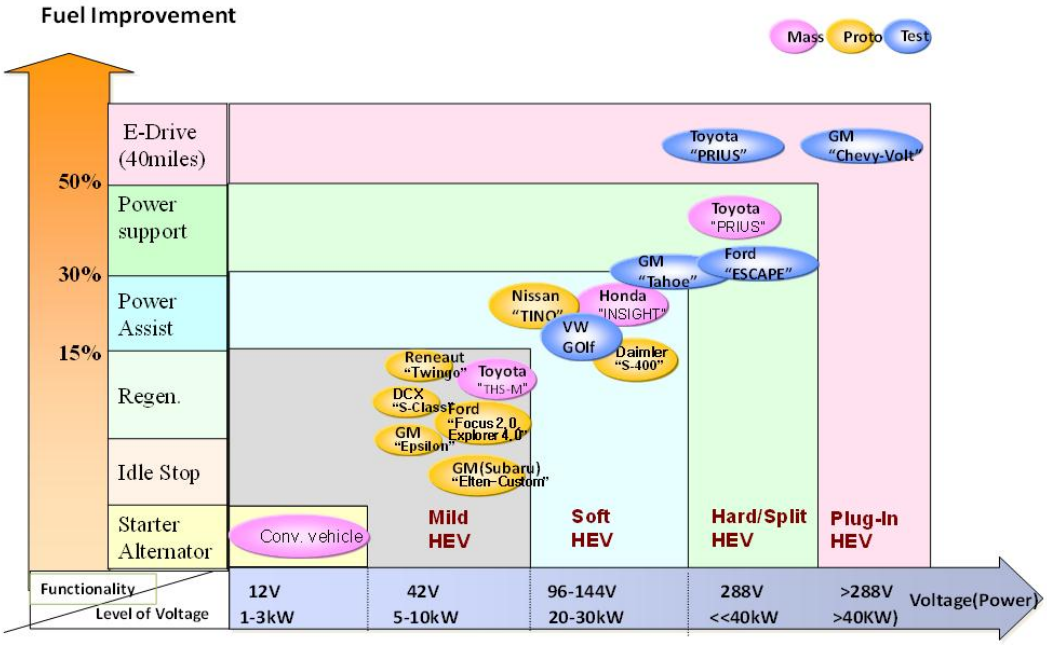

Figure 2: Trend of HEV propulsion system development (from Dr. Song-yul Choe, unpublished)

Other than high electrical power, mechanical vibrations, thermal cycling and humidity that a car undergoes can also cause degradation and failure of the connectors. If the connector contacts degrade, the contact resistance can increase and cause other problems with the power electronics and controls of the electrical power drive system. Eventually, connectors could catastrophically fail and become either permanently welded together or effectively non-conductive.

The main motivation of the current study is to research the performance of connectors for HEV vehicles under these realistic operating conditions experimentally and theoretically. To emulate these conditions, a test stand for the 300A-rated connector was designed which facilitates the supply of high current, generation of vibration and control of environmental temperature with the measurement of connector resistance (R_C), connector temperature (T_C) and connector motions.

Based on the results of the experimental study, increase of connector resistance is most likely to occur from vibration in the direction perpendicular to cable axis. In addition, more change in connector resistance occurs at higher vibration amplitudes, frequencies and lower ambient temperatures. A micro-roughness surface analysis of the silver coating connectors shows that the defect area on the surface is best referred to as a worn pit rather than corrosion because the main finding is indentation and removal of the coating material.

According to the experiments, vibration is the most significant cause the increase of connector resistance, compared to current rate and ambient temperature. The experimental results show that the increase of connector resistance under vibration is primarily due to the relative displacement between male and female parts of the connector, rather than fretting corrosions. Finite element models are used to analyze this phenomenon and compare with experimental results. A two dimensional finite element model is developed to describe the overall connector system with a capability of calculating relative displacements between the female part and male part at the contact surfaces. Contact spring present between the female and male parts of the connector is modeled in three dimensions and used to analyze time responses of the spring.

The two dimensional finite element models show that the relative displacement between the female part and male part at the contact surfaces is closely related to the changes of connector resistance under vibration. A prominent finding is made from the three dimensional model, which shows that contact surfaces of each contact pair do not have the identical motion under vibration, and the gaps between the contacts are found. It is assumed that these contact gaps causes connector resistance to increase and oscillates during vibration because they may induce capacitance or electric arcing between the contacts. With the validation of experimental results, it is proved that the models are powerful to aid in fundamental characterization, prototype evaluation and design of high power connectors.

CHAPTER 2 LITERATURE REVIEW

Automotive connectors experience a harsh environment comprised of vibrations induced by the engine, thermal cycling as the vehicle starts up and shuts down, and a corrosive environment which can cause the formation of undesired oxides [1]-[2]. These conditions are very demanding on the reliability of connectors and often lead to degradation and failure. A vehicle may have more than 400 connectors with 3000 individual terminals but field data has shown that connector degradations and failures contribute to 30–60% of the electrical problems [3]-[4]. This requires investigations on connector behavior under vehicle conditions and studies on its degradation mechanisms so that connectors perform on an acceptable level.

2.1 The effect of vibration on fretting corrosion

For connectors subject to vibration, a main degradation mechanism is fretting, which is a relative cyclic motion with small amplitude that occurs between two oscillating surfaces, defined by Waterhouse [5]. Varenberg et al. also characterized fretting in terms of the local relative motion [6]. Fretting is generally found to cause intermittent electrical contact, wear and corrosion on contact materials and in turn results in variations of electrical contact resistance such as an increase, fluctuation or intermittence.

Fretting corrosion has been extensively investigated by many researchers. During fretting corrosion, fretting wear repeatedly exposes fresh metal to the atmosphere which causes oxidation and the accumulation of debris on the contact interface. This continuously reduces the electrical conducting area and conductivity [7]-[9]. Consequently, when vibration is applied, the contact resistance will continue to increase gradually with time [7], [9]-[15]. Many works report that the

degradation of the contact interface will cause the contact resistance to increase greatly with sudden failure after a certain number of vibration cycles [7], [11]-[12], [14]. These phenomena are mostly observed on electrical contacts with conventional coatings, such as tin [7], [9]-[15].

2.2 The effect of vibration on temporary changes of contact resistance

However, superimposed on the gradual increase of contact resistance, various studies also show that the contact resistance may increase temporarily and significantly, and then oscillate synchronizing with the vibration [14], [16]-[25]. This phenomenon is extremely obvious in our vibration tests where silver-plated connectors are used. When vibrations start, the connector resistance significantly increases and oscillates. When the vibrations are stopped, the resistance is set back to a value that is similar to the original state. It is the relatively stable property of silver that makes fretting corrosion less significant so that the temporary changes of contact resistance dominates the experimental results.

The temporary changes of the contact resistance are dependent upon operating conditions. One of the reasons is the wear debris and particles formed at the contact surface [14], [16]-[17]. Hubner-Obenland and Minuth found the periodical alternations of contact resistance for various contact materials subject to vibration [14], which is caused by debris of a degraded contact which behaves like a potentiometer with the least resistance at the rest position of the contact. Carvou and Jemaa also found out that when the contact surface moves along the track formed by oxide particles, contact resistance varies periodically under vibration [16]. Skinner concluded that particles in order of 25μm between the contact terminals lead to changes in contact resistance and even disturbance of intermittence [17].

On the other hand, periodic separations of contact surface, or contact gaps, also cause temporary increase and oscillation of contact resistance [18]-[21]. This phenomenon is commonly found on electrical connectors, relays and switches which may cause electrical arcing. Mcbride used a mathematically modeled contact bounce to show that the contact separations are small such that the minimum arc voltage is maintained [18]. Ben Jemaa et al. found that the electrical arcing causes contact resistance enhanced progressively and started to demonstrate high fluctuations under vibrations [19]-[20]. The arcing voltage is due to bounce phenomena between the contacts under vibrations [19]. In addition, periodic separation of contact surface may vary capacitance between the two contact surfaces, which was measured by Kopanski for for a lithographic overlay subject to vibration [21].

When the changes of contact resistance are associated with short duration discontinuities, it is defined as intermittence [22]-[25]. According to a study on intermittence detection by Murrell and McCarthy, the contact resistance remains high throughout most of the cycling but fluctuates by several orders of magnitude after 10,000 cycles with the presence of significant intermittences [22]. The reasons of intermittence are not limited to wear debris buildup [23]-[25]. Maul, McBride and Swingler provided explanations that the contact area should be small at the time when intermittence (or discontinuity) occurs, and the current density in the contact region is very high [23]. This mechanism of intermittence is explained using a model by Malucci, where cold welded asperities are stretched or sheared during relative motion of the contact terminals [24]. Other author like Maul and McBride interpreted the intermittence as the temporary disruption of metallic conduction in a closed electrical contact [25].

2.3 The effect of ambient temperature and humidity on fretting corrosion

The effect of temperature on fretting is another important consideration for connector failures. Y. W. Park et al. found that temperature has a great influence on the fretting corrosion of the tin-plated contacts [9]. Relatively higher temperatures tend to soften the contacting asperities of tin resulting in less fretting wear. However, high temperatures will also increase the rate of oxidation and then accelerate fretting corrosion. In addition, sliding friction in a connector leads to a temperature rise and it may be a major source of electrical contact deterioration. In 2009, Chen et al. created a model that is able to capture the inception of material melting temperature rise caused by sliding friction [26].

The corrosion of automotive connectors can be exacerbated by humidity in vehicles [27] and the influence of humidity varies greatly for different coating materials [11], [28], where the experimental results show that silver coatings have much longer life times with humidity conditions than any other coating materials. Therefore, the power connectors with silver-coatings appear to be a good candidate for automotive applications. Bruel [28] found that the contact resistance of silver was much more stable than copper, brass and nickel, under the humidity environment with applied sliding. Rudolphi and Klafke [12] also found that silver and gold are the excellent candidates since they have the lowest resistance increase under sliding and humidity conditions.

2.4 Measurement techniques and analysis using (FEM)

Since the investigations of the connector performance are mostly realized by accelerated tests, a precise measurement can help to better characterize connector fretting and degradation mechanisms. It is recommended to use high sampling rate of measuring contact resistance under

vibration to characterize a complete waveform of the contact resistance [19], [23], [27]-[28]. Proper instruments are also inevitable for obtaining fretting mechanisms in experimental tests. In 2003, Flowers et al. used non-contacting laser vibrometer to measure relative displacement of contact interface to predict the fretting corrosion of tin-plated connectors [29]. They found that the relative motion of contact interface is proportional to the increase rate of contact resistance.

Some authors used finite element methods (FEM) to analyze electrical contacts [30]-[32]. For example, Xie [30] and Chen [31] used it for analysis of dynamics and fretting of connector subjected to vibration and Zhai et al. used it for anlaysis of dynamic characteristics of pick-up and drop-out process of contact of electromagnetic relay [32]. However, computational time increases drastically to calculate dynamic characteristics of connectors using a three-dimensional model [31]. Thus, to minimize the computational cost, we developed a two-dimensional model for the connector system that embeds a detailed three-dimensional model for the contact spring. The model is used to analyze effects of vibrations on the contact surfaces. Experiments are conducted to verify the numerical analysis.

CHAPTER 3 HIGH POWER CONNECTOR AND EXPERIMENTAL SETUP

3.1 Specification for high power connector

Connectors used for experiments are made of male and female parts contacted by a spring that allows for absorbing mechanical vibrations while maintaining a high conductivity, which is manufactured by LS Cable™ and shown in Figure 3 (a). The connector has a cylindrical form. The male part has a pin with a round shape (Figure 3 (d)), while the female part has a tube form (Figure 3 (b)) where a ring-shape spring punched from sheet metal is mounted inside the female connector (Figure 3 (c)). The spring serves to produce contact pressure perpendicular to the surface of the male and female parts by contact tabs. These contact pressures compress each of tabs in the radial direction and provide electrical connections between the female and male parts of the connector. The specification and material properties of the connector for 300A current rating is listed in Table 1. The connector surface is plated with silver, while the bulk connector material is made of copper alloy. The connector system in testing also includes housing and supplied cable, which will be shown in a later section.

(a) Connector mate

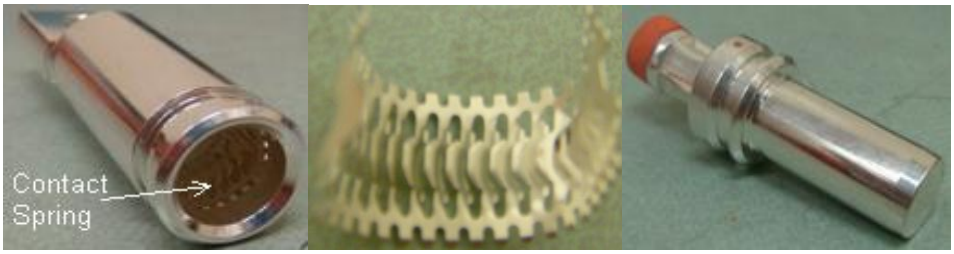

(b) Female part with cont (c) Contact spring (d) Male part

Figure 3: Geometrical structures of the connector

Table 1: Specification of the connector

Components	
Material properties	
Bulk material	Copper alloy
Young's modulus (GPa)	117
Poisson's ratio	0.34
Mass density (kg/m^3)	8930
Surface plating	Silver
Friction coefficient	0.34
Dimensions	
Overall length (mm)	105.3
Outer diameter (mm)	20.1
Current rating (A)	300

3.2 Experimental Setup

3.2.1 Design of test stand

In order to investigate connector performance and reliability, a connector test stand design is developed to represent real operating condition and provide a controlled testing environment. A high DC current is supplied for the connector under a controlled environment with desired vibration, temperature and humidity conditions. The test stand facilitates the measurement of connector resistance, R_C, and connector temperature. T_C, during the tests and the measured data are processed and displayed in real time. A schematic diagram of the designed test stand is depicted in Figure 4.

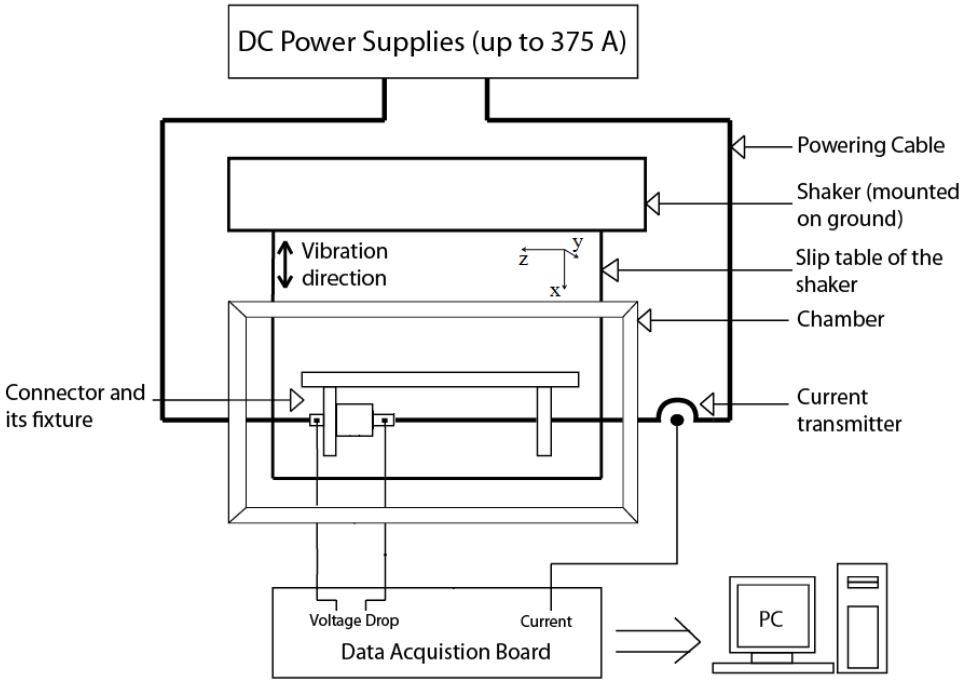

Figure 4: Schematic diagram of test stand

3.2.2 Design of electrical and mechanical hardware

To provide a power source for the connectors, three Sorensen DCS-125E power supplies are selected. The maximum current output of each power supply is 125 A. Multiple power supplies can be wired in parallel resulting in a maximum current of 375A, as shown in Figure 5. The power supply is able to be remotely controlled by PC to output the desired current value and complex profile as needed.

Figure 5: Testing System Rack with Parallel Power Supplies (above the PC)

Vibration tests are performed using an amplitude-and-frequency-controlled electro-magnetic shaker and environmental chamber, which enclosed the connector to be tested, as shown in Figure 6. The LDS V850 Shaker is able to output any vibration amplitude and frequency combination with a maximum G-value of 30g. A CSZ environmental chamber is used

to control the ambient temperature and humidity of the enclosed connector. The temperature range can be set from -20 to 400°C, with 0-100% relative humidity. The chamber is placed above the shaker so that the connector can be enclosed as shown in Figure 6 (b).

(a) LDS V850 Shaker

(b) CSZ environmental chamber

Figure 6: Vibration Shaker and Environmental Chamber

The connector to be tested is placed in the chamber. Fixtures are especially designed to secure the connector on the shaker through the cloth that is used to insulate the inner temperature and humidity from room environment, as shown in Figure 7. The power supply cable goes through the hole on top of the chamber and then connects to the power source. The measuring wires of voltage and thermocouple also go through the same hole and then connected to data acquisition board.

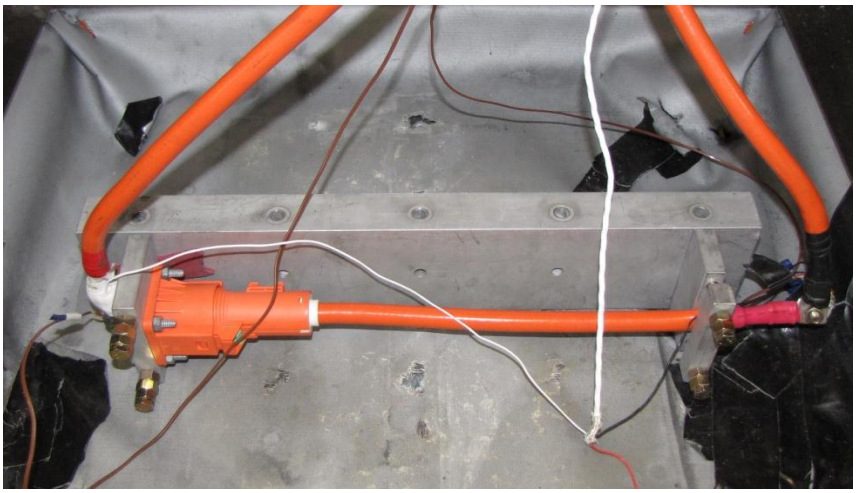

Figure 7: Fixture of connectors on the shaker, enclosed by chamber

The test fixture secures the connector housing so that the connector vibrates in the same way with the shaker. The clamp is designed to fix the supplied cable to the shaker. The base of the fixture is designed with multiple sets of holes so that the position of the clamp can be adjusted for different lengths of the cable. In this way the natural frequency of the connector system can be adjusted if needed. Having longer cables involved in vibrating system results in lower natural frequency.

3.2.3 Instruments

Within a controlled environment at a specified vibration direction, amplitude, frequency and ambient temperature, connector performance and degradation characteristics can be obtained by measuring R_C, T_C, and motions. The analog signals of voltage drop and transmitted current are collected by National Instrument™ analog input modules, shown in Figure 8. The temperature readings are collected by thermocouple input modules. The modules are installed in a data acquisition board placed in the system rack, as shown in Figure 5. All the signal measuring wires are shielded to minimize electrical magnetic interference (EMI). The measuring wires also go through magnetic ferrites to further remove EMI, and all power cables are grounded.

Figure 8: Data acquisition board with AI modules

3.2.3.1 Measurement of R_C and T_C

R_C is indirectly estimated by measuring the voltage drop of the connector and DC current in the power loop and then by applying ohm's law: $R_C=V_C/I_C$. The locations of measuring

voltage drop of connector, V_C, are shown in Figure 9. One voltage measuring wire is soldered on a metal eyelet that is firmly fixed on the connector terminal by bolt, as shown in Figure 10. The other voltage measuring wire is firmly stuck between the right end of male part and cable. This is the best way to ensure measurement precision and repeatability.

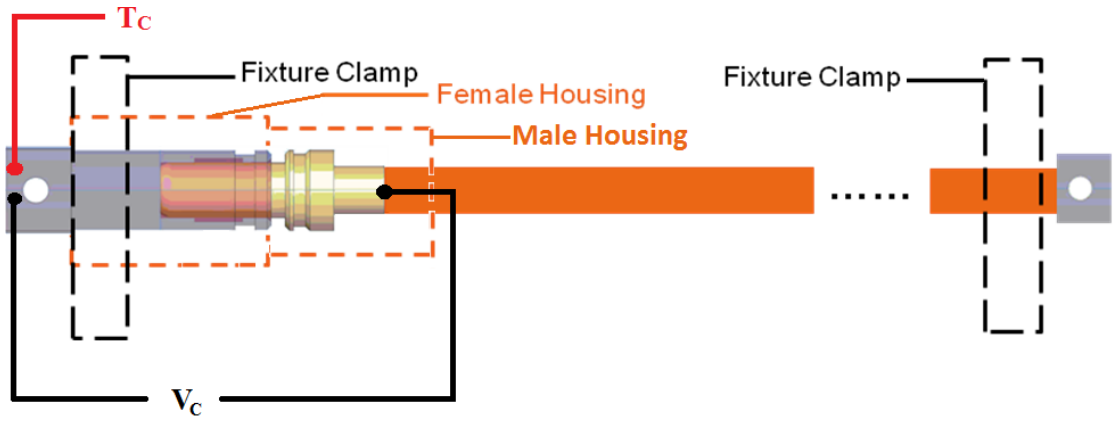

Figure 9: Locations of measurements of voltage drop (V_C) and connector temperature (T_C)

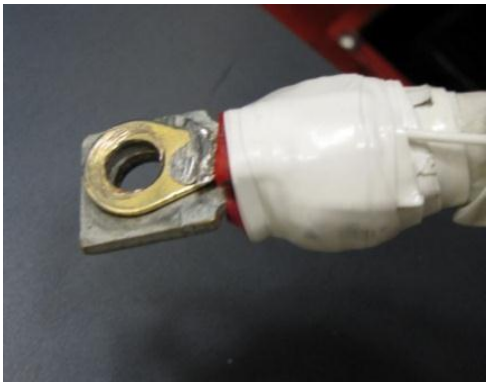

Figure 10: Metal eyelet for measuring voltage and temperature

The current going through the connector, I_C, is measured by a LEM IT 400-S current transmitter, as shown in Figure 11. This device converts the current into analog signals that can be logged by analog input modules. The connector temperature, T_C, is measured by K-type

thermocouple. The probe of thermocouple is also soldered on metal eyelets and fixed on the connector terminal, as shown in Figure 10.

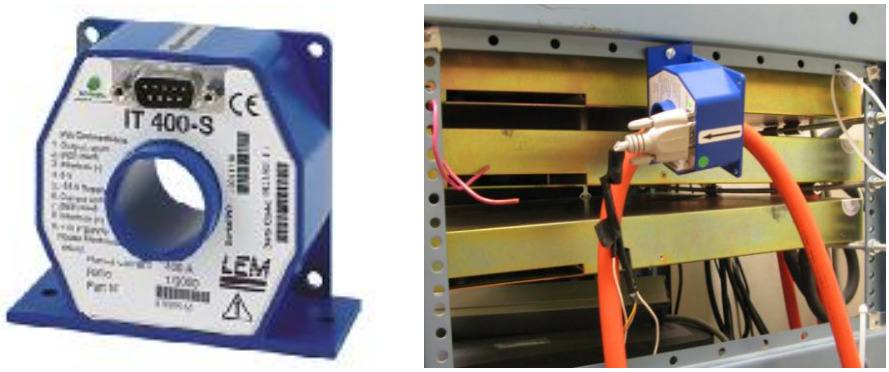

Figure 11: LEM IT 40-S Current Transmitter

3.2.3.2 Measurement of motions

The measurement of the motions of the connector is carried out using Polytec non-contact laser vibrometer system. The system contains two vibrometers and each one has an OFV 353 sensor heads (laser) and a OFV 2610 controller, as shown in Figure 12. The sensor heads are supported by tripods, as shown in Figure 13, and point to a location of interested on the connector during vibration. The analog signal can be obtained at the vibrometer system's output that is proportional to the vibration amplitude of the measured location.

Figure 12: Non-contacting laser vibrometer system with sensor head and controller

(a) Photograph of the setup of vibrometers

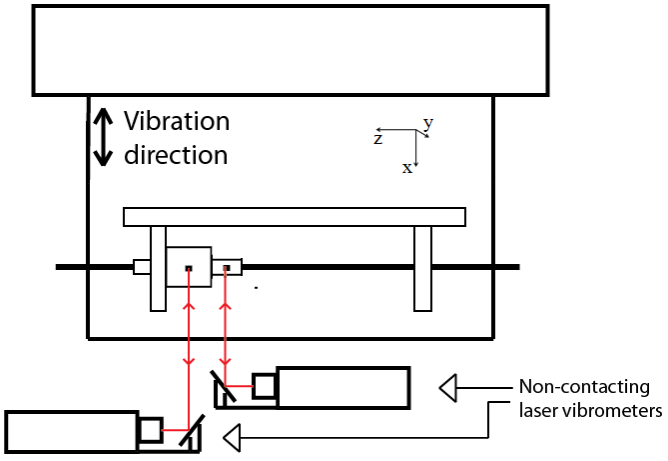

(b) Schematic diagram of the setup of vibrometers

Figure 13: Setup of non-contacting laser vibrometers

Each vibrometer can be used to measure the magnitude of motion at one location of the connector system. When one vibrometer is considered as the reference, the other one can also measure the phase shift of the motion. Each motion is given as a polar form in following equation:

$$U_i = M_i \sin(\omega t + \varphi_i) = M_i \angle \varphi_i \quad (1)$$

where M_i is the magnitude and φ_i is the phase shift of the motion U_i. i is a value from 0 to 4, which corresponds to 5 different locations of the connector system, which be shown in Chapter 5 and 6.

3.2.3.3 Measurement of surface profile

The surface of the tested connector can be measured for the investigation of wear and degradation. An optical stylus profilometer is available to measure the surface profile and roughness for both 40A and 300A connectors, as shown in Figure 14.

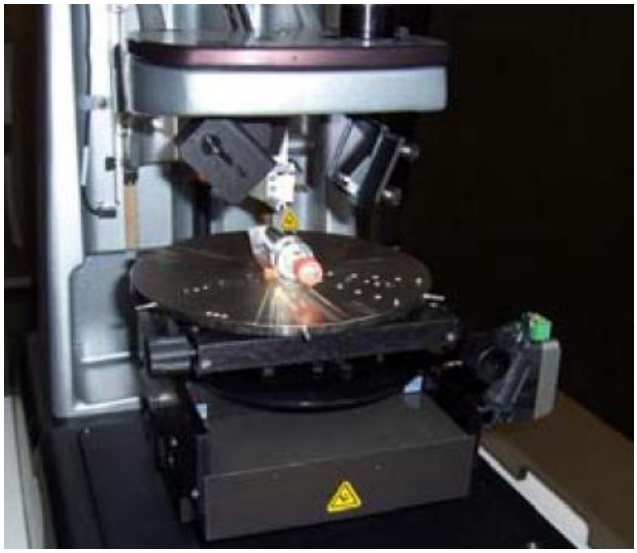

Figure 14: Surface profilometer

3.2.4 Calibrations, uncertainty of measurement and EMI

Calibrations are implemented to improve measurement accuracy. An Agilent 34411A high precision multimeter, as shown in Figure 15, is applied to calibrate all analog input modules. The calibration data is shown in Figure 16, which includes the readings of analog input module and the multimeter over the measurement range.

Figure 15: Agilent 34411A multimeter for calibration

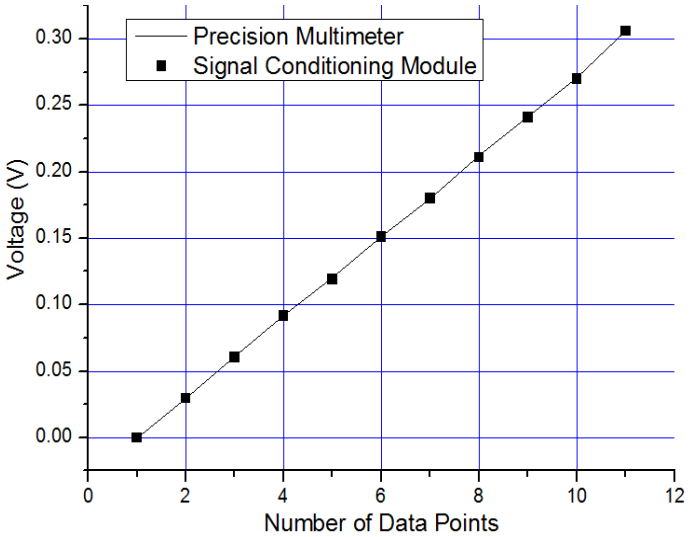

Figure 16: Calibration data of analog input modules and precision multimeter

An ice point reference, shown in Figure 17, is used to calibrate the thermocouples. The ice point reference is able to maintain 0 ±0.1 °C in the wells where probes can be inserted in. By noting the temperature difference between the thermocouple reading and the freezing point, the thermocouple is calibrated and its accuracy can be improved.

Figure 17: Ice point reference used to calibrate thermocouple

After the instruments are calibrated, the uncertainty of measurements are calculated and listed in Table 2, using the equation of error propagation.

Table 2: Uncertainty of measurement after calibration without considering other disturbances

	Voltage drop	Current	Connector resistance	Connector temperature
Accuracy	0.0037mV (0.08%)	0.047A (0.02%)	0.018μΩ (0.09%)	0.1%

The calculation of measurement uncertainty shown in Table 2 has not considered the effect of EMI, which is probably caused by the electro-magnetic shaker. In order to estimate the disturbance of EMI on the measurement data in vibration tests, a vibration pretest is conducted

and the resistances of connector and cable are both measured. As shown in Figure 18, the data measured at the connector varies during the vibration, and the data measured at the cable is constant during the vibration. Since both connector and cable are exposed to vibration, the constant data shown in Figure 18(b) demonstrates that the disturbance of EMI from the shaker is negligible, and the variation of data shown in Figure 18(a) is caused by the actual changes in connector resistance.

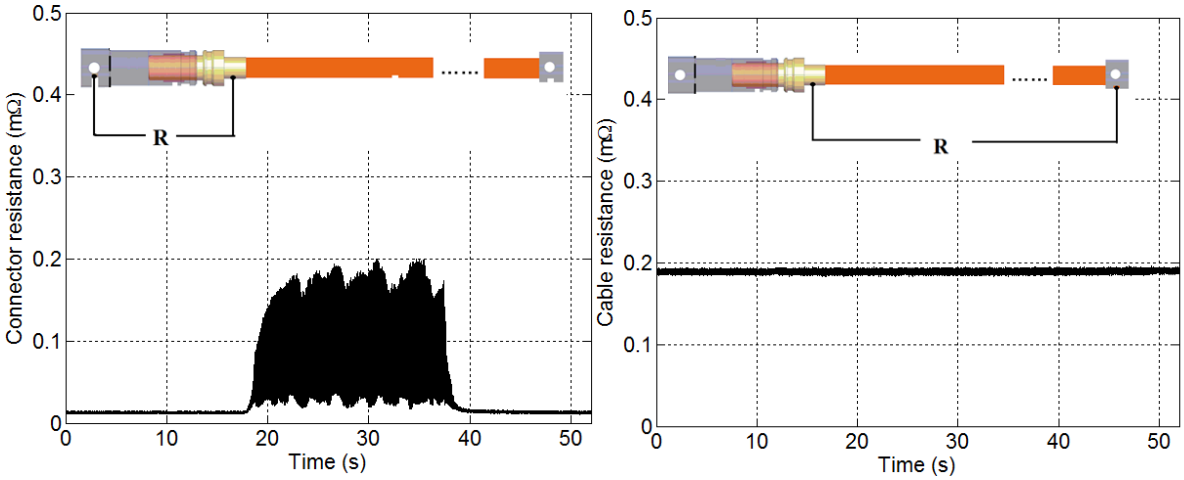

(a) Connector resistance (b) Cable resistance

Figure 18: Comparison of connector resistance and cable resistance under a vibration pretest (Vibration amplitude: 0.18mm, frequency: 240Hz, duration: 20s)

CHAPTER 4 ACCELERATED TESTS UNDER VARIOUS TESTING CONDITIONS

4.1 Methodology of accelerated tests

4.1.1 Test conditions

This chapter studies the effect of various operating conditions on connector performance, which is summarized in Figure 19. Vibrations will be applied to the connectors with different direction, amplitude and frequency. At the same time, ambient temperature can be also controlled. The connector performance, fretting and failure mechanism are primarily estimated by connector resistance, R_C. Connector temperature, T_C, will be also studied as an auxiliary assessment.

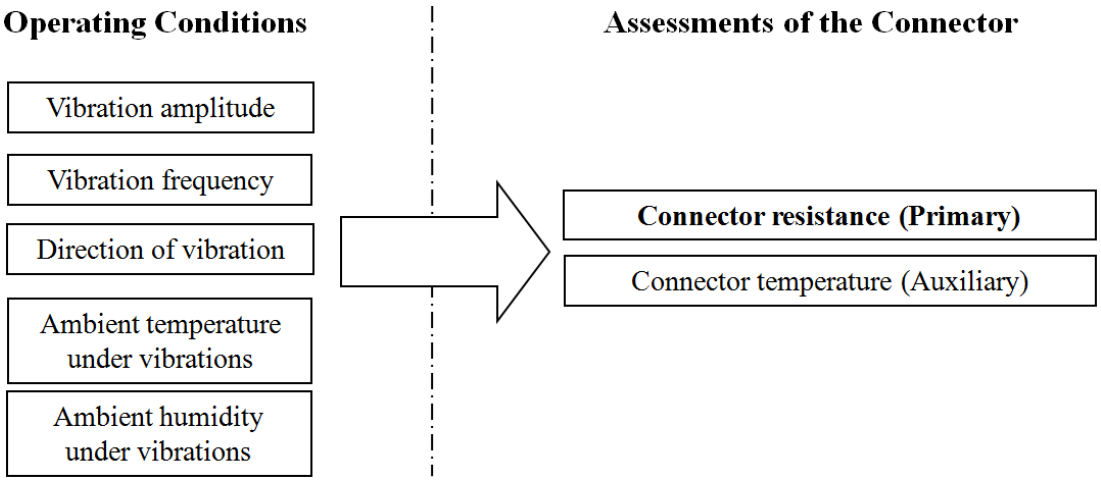

Figure 19: Operating conditions and assessments of connector for accelerated tests

4.1.2 Definition of coordinates for vibrations

The definition of coordinate is shown in Figure 20. Z direction follows the direction of cable. The X and Y direction are perpendicular to the Z direction via the right hand rule. For the symmetric nature of connector, vibrations in X and Y directions are identical so that the vibration in Y direction is neglected for the connector.

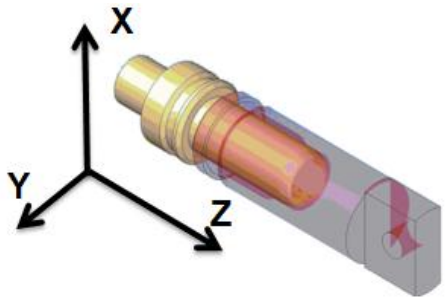

Figure 20: Definition of coordinates for vibrations

4.1.3 Test procedure and test matrix

The test procedure for each test run is defined in Figure 21. Before vibration starts, the connector should be fully heated by the constant applied current of 220A with controlled ambient temperature environment.

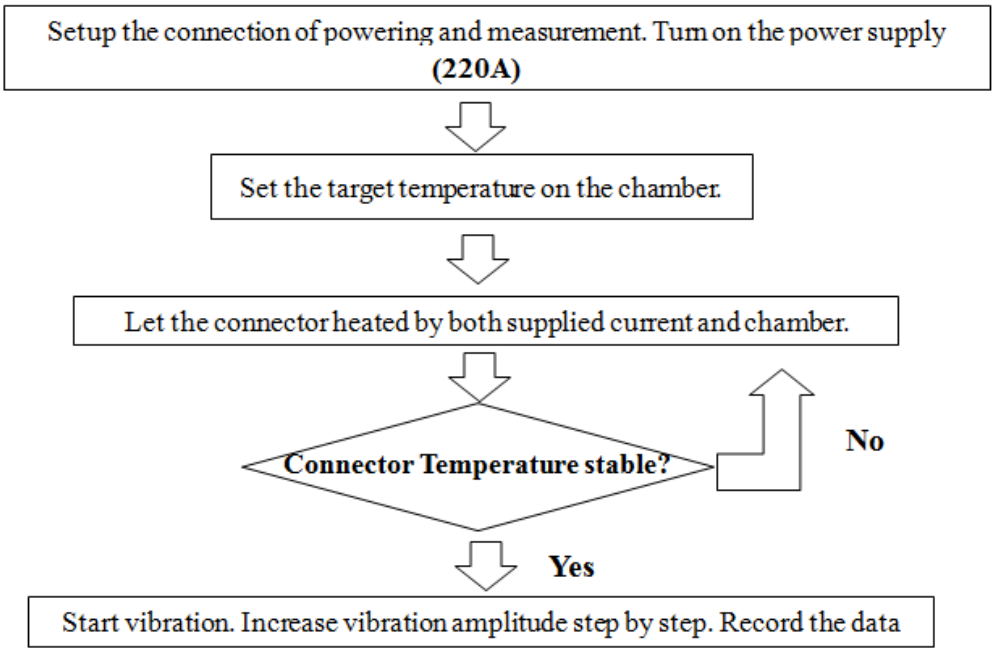

Figure 21: Test procedure for accelerated tests

Detailed test conditions for each test run are listed in the test matrix, as shown in Table 3. A new connector will be used for each test run. Three repeating iterations for each test run are required to study the repeatability of data.

Test 1 is the benchmark test and all other test runs make changes of certain operating condition based on Test1. Test 2 and 3 change the direction of vibration. Since the connector is symmetric in X and Y direction, test 3 is neglected. Test 4, 5 and 6 change the vibration frequency. Test 7 and 8 change the ambient temperature. Test 9 and 10 are supposed to change the humidity. However, the effects of humidity on silver-plated connectors can be neglected because silver is much more stable than other conventional materials under the humidity environment [12], [28]. Therefore, Test 9 and 10 are neglected. Test 11-14 change vibration frequency and ambient temperature simultaneously.

Table 3: Test matrix of accelerated tests

Test Run	Frequency (Hz)	Temperature (0C)	Vibration Directions	Comments
1	100	80	Z	Benchmark Test
2	100	80	X	Vary direction of vibration
3	Y direction vibration test is neglected because of symmetry with X			
4	50	80	Z	Vary vibration frequency
5	150			
6	200			
7	100	25	Z	Vary temperature
8		120		
9	Tests of humidity effect are neglected for 300A connectors (silver coating)			
10				
11	50	25	Z	Vary frequency and temperature
12	200	25		
13	50	120		
14	200	120		

For each test run, the vibration amplitude is increased step by step, as shown in Table 4. Vibration is applied for 3 minutes at each amplitude, and held for 1 minute before starting the next one. For the tests with vibration frequency higher than 100Hz, the maximum vibration amplitude cannot reach 0.8mm because it is limited by the shaker capability.

Table 4: Vibration amplitudes (peak-to-peak) for each test run

Vibration Amplitudes (mm). 3 minutes for each amplitude with 1 minute break in between										
0.05	0.1	0.15	0.2	0.25	0.3	0.4	0.5	0.6	0.7	0.8

4.2 Methodology of accelerated tests

4.2.1 Experimental results of R_C

4.2.1.1 Baseline data of R_C without applying vibration

The baseline data of R_C are collected before vibration starts in each test run. Without vibration, R_C is only dependent on ambient temperature under constant current. These baseline data are averaged in all tests and plotted versus ambient temperature, as in Figure 22, where the error bars show the standard deviations. It is shown that the R_C increases slightly with the increase of ambient temperature, which is mostly caused by the bulk resistance of the male and female parts.

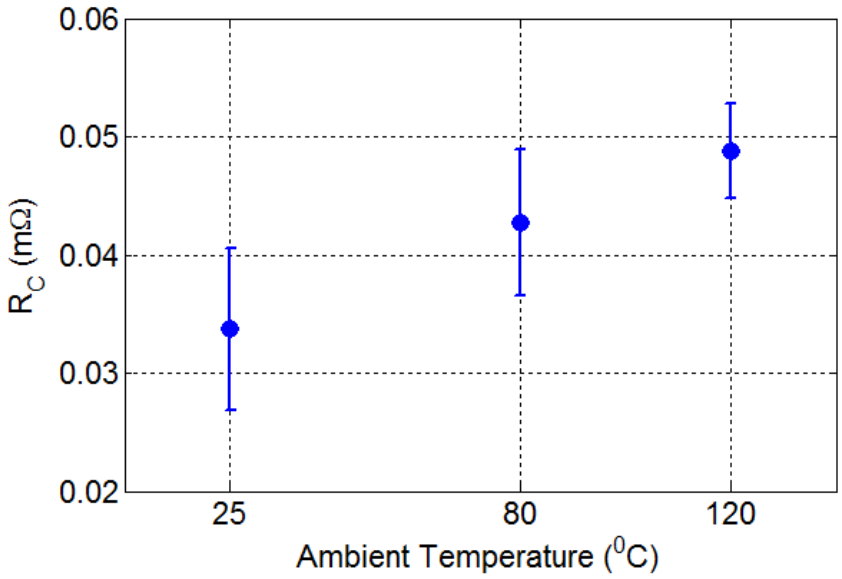

Figure 22: Averaged R_C under different ambient temperatures without vibration

4.2.1.2 ΔR_C with all operation conditions

The change of connector resistance, ΔR_C, is defined as the average value of connector resistance under vibration subtracted by the value before vibration starts. The R_C under each vibration amplitude can be simplified to one value of ΔR_C, so that one test run has a series of ΔR_C. For example, the data of R_C in the 1st test run of 3rd iteration is shown in Figure 23, where ΔR_C are marked when vibration amplitudes are 0.3mm, 0.5mm and 0.8mm.

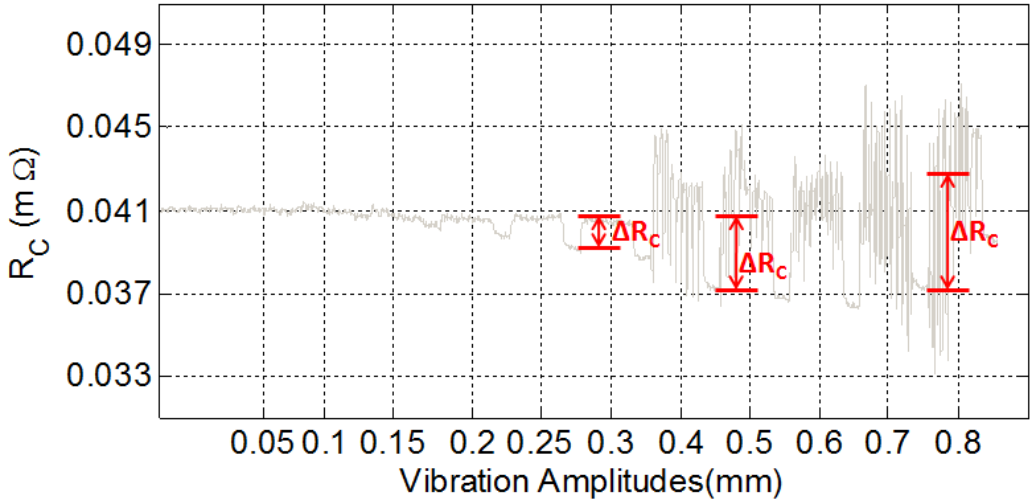

Figure 23: Definition of ΔR_C

Since each test run (shown in Table 3) is conducted three times repeatedly, the ΔR_C are averaged among the repeating tests and plotted from Figure 24 to Figure 27. In addition, the standard deviations of ΔR_C among the repeating tests are calculated and will be presented as error bars.

The ΔR_C for test 1 and 2 are plotted in Figure 24 to study the effect of direction of vibration. The data shows that ΔR_C has an increasing trend with the increase of vibration amplitudes. The vibration in X direction causes more of an increase in connector resistance compared to vibration in Z direction.

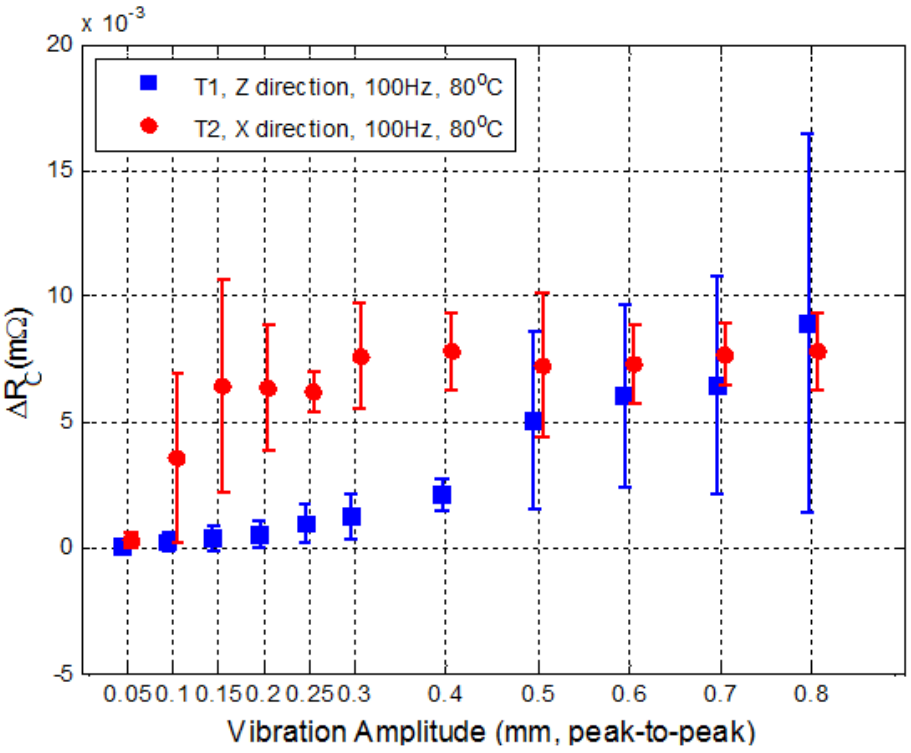

Figure 24: ΔR_C under different vibration directions (Test 1 and 2)

The ΔR_C for test 1, 4, 5 and 6 are plotted in Figure 25 to study the effect of vibration frequency. The data shows that higher frequency vibrations cause more of an increase in connector resistance compared to vibrations at lower frequencies. Due to the limitation of shaker capability, the vibration amplitudes at 150Hz and 200Hz cannot reach 0.8mm.

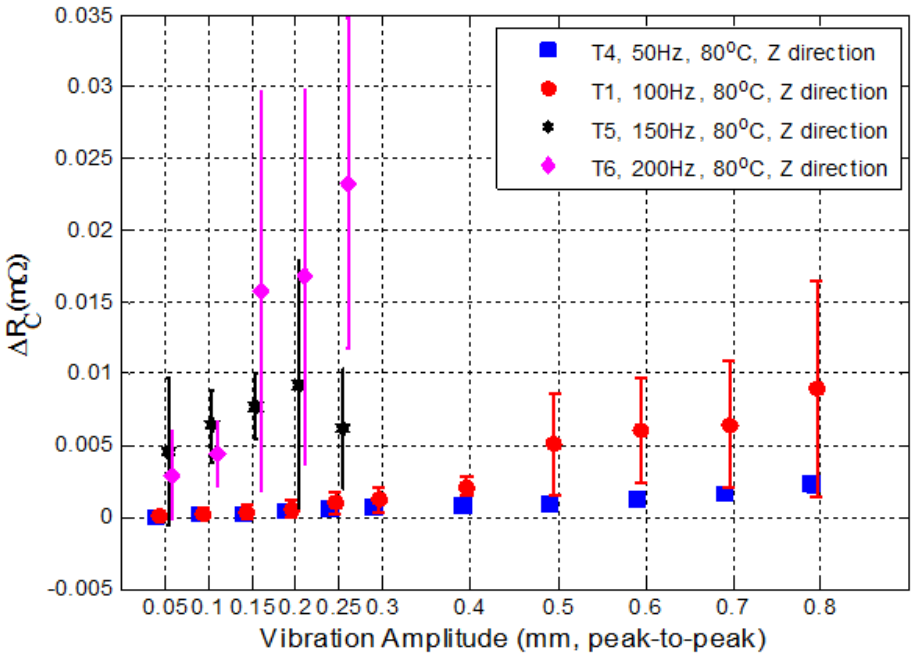

Figure 25: ΔR_C under different vibration frequencies (Test 1, 4, 5 and 6)

The ΔR_C for tests 1, 7 and 8 are plotted in Figure 26 to study the effect of ambient temperatures. The data shows that the vibrations at lower ambient temperatures cause more of an increase in connector resistance compared to the vibrations at higher ambient temperature.

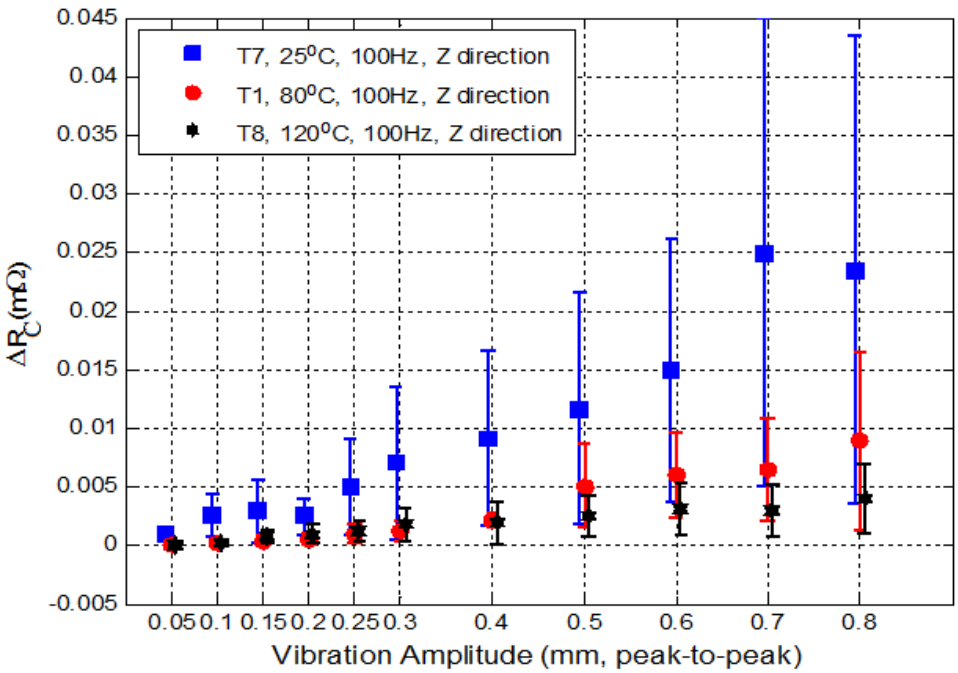

Figure 26: ΔR_C under different ambient temperatures (Test 1, 7 and 8)

The measured ΔR_C values for test 11, 12, 13 and 14 are plotted in Figure 27 to study the effect of vibration frequency and ambient temperatures. Again, the data shows that vibrations in higher frequency and lower ambient temperatures cause more of an increase in connector resistance.

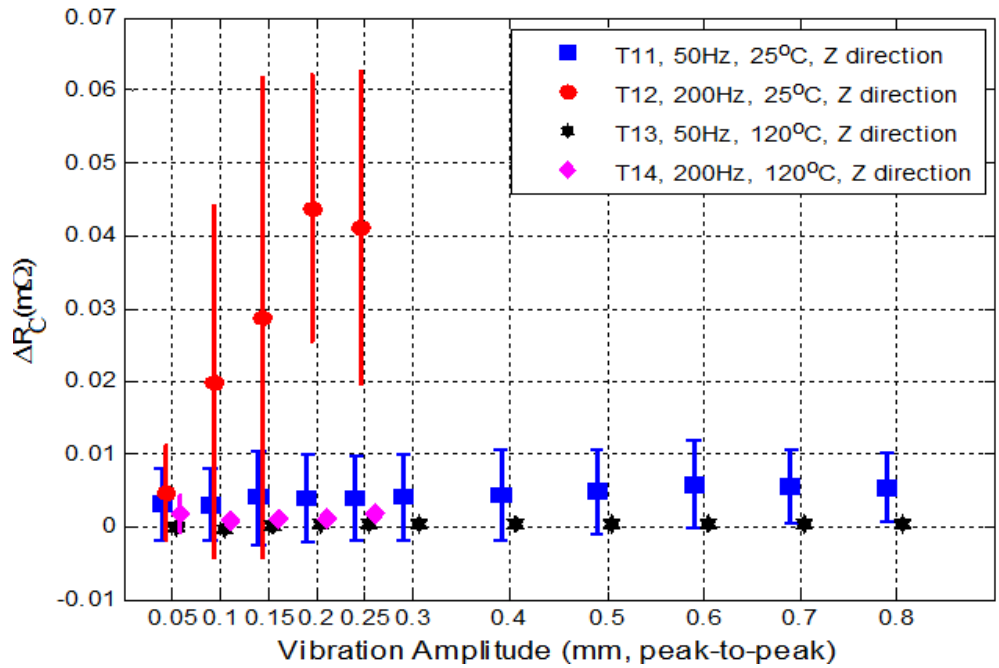

Figure 27: ΔR_C under different vibration frequencies and ambient temperatures (Test 11, 12, 13 and 14)

4.2.2 Experimental results of T_C

4.2.2.1 Baseline data of T_C without applying vibration

Similarly, the baseline data of T_C are collected before vibration starts in each test run. Without vibration, T_C is only dependent on ambient temperature under constant current. These baseline data are averaged in all tests and plotted versus ambient temperature in Figure 28, where the error bars show the standard deviations. It is shown that the T_C is always approximately 20˚C higher than the ambient temperature. This must be caused by Joule heating when the current goes through the connector and cable.

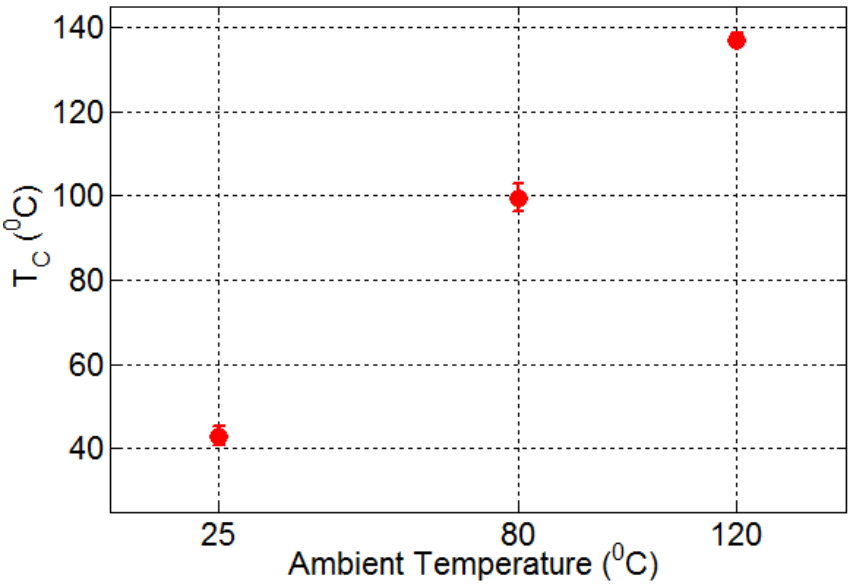

Figure 28: T_C under different ambient temperatures without vibration

4.2.2.2 ΔT_C with all operating conditions

The change of connector temperature under vibration, ΔT_C, is defined as the overall increase of connector temperature over the entire test run. Since T_C is an auxiliary factor to assess connector performance, each test run has only one ΔT_C to represent the changes in connector temperature. For example, the data of T_C in the 1st test run of 3rd iteration is shown in Figure 29, where ΔT_C is marked as the overall increase of connector temperature during the entire vibration.

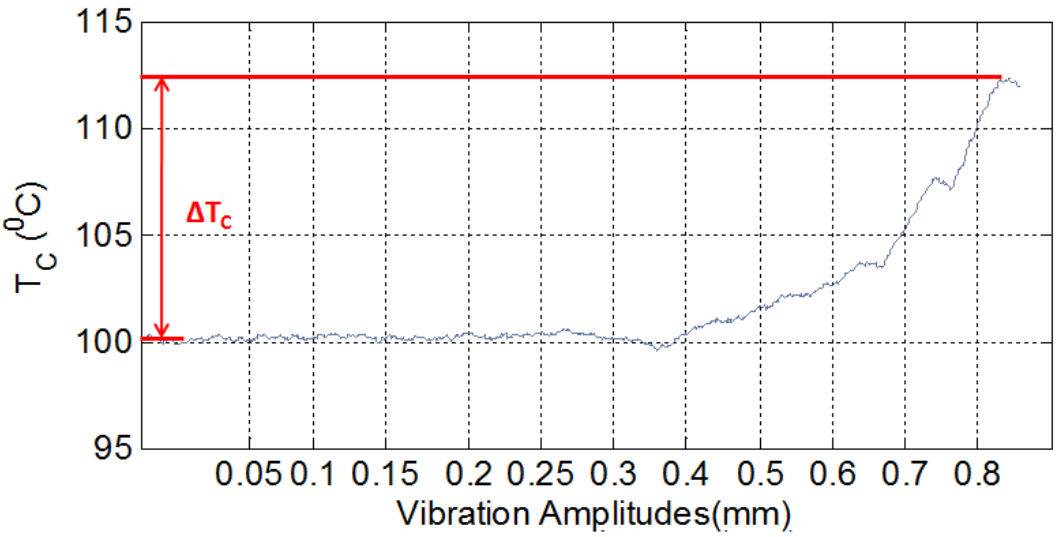

Figure 29: Definition of ΔT_C

Since each test run is conducted three times among repeatedly, the ΔT_C are averaged among the repeating tests and plotted from Figure 30 to Figure 33. In addition, the standard deviations of ΔT_C among the repeating tests are calculated and will be presented as error bars.

The ΔT_C for tests 1 and 2 are plotted in Figure 30 to study the effect of direction of vibration. The data shows that the ΔT_C in the Z direction is slightly larger than the X direction. However, the standard deviation of ΔT_C is large, which means that the temperatures in different vibration directions may not be statistically significant.

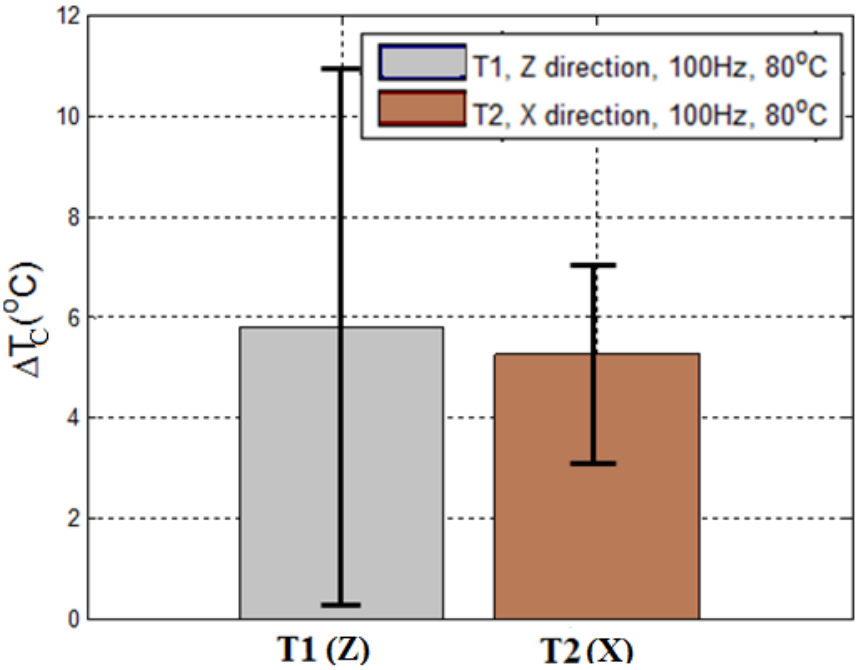

Figure 30: ΔT_C under different vibration directions (Test 1 and 2)

The ΔT_C for tests 1, 4, 5 and 6 are plotted in Figure 31 to study the effect of vibration frequency. The data shows that higher frequency vibrations cause more of an increase in connector temperature in general, although the ΔT_C in 150Hz is slightly larger than that in 200Hz. Since the maximum vibration amplitude for T5 and T6 is 0.25mm, the ΔT_C for T1 and T4 is also calculated at 0.25mm in this figure.

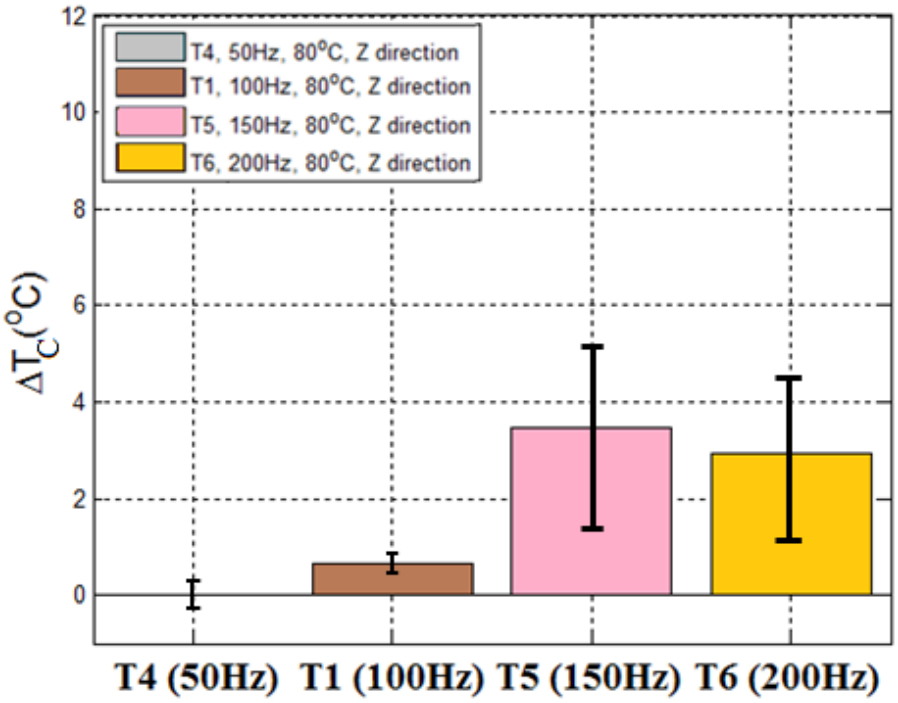

Figure 31: ΔTC under different vibration frequencies (Test 1, 4, 5 and 6)

The ΔT_C for tests 1, 7 and 8 are plotted in Figure 32 to study the effect of ambient temperatures. The data shows that ΔT_C is largest in test 1 and smallest in test 7 and that the repeatability of data is not good. It means that the connector temperatures under vibration at different ambient temperatures may not be statistically significant.

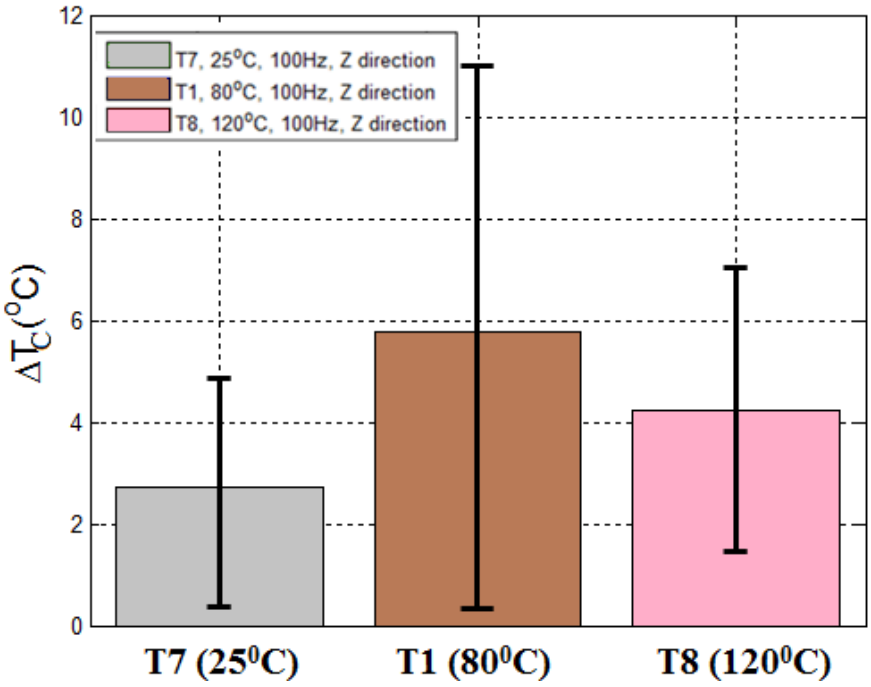

Figure 32: ΔT_C under different ambient temperatures (Test 1, 7 and 8)

The ΔT_C for tests 11, 12, 13 and 14 are plotted in Figure 33 to study the effect of vibration frequency and ambient temperatures. It is shown that higher frequency vibrations cause much more of an increase in connector temperature but also that the effect of ambient temperature does not have a statistically noticeable effect on ΔT_C. Since the maximum vibration amplitude for T12 and T14 is 0.25mm, the ΔT_C for T11 and T13 is also calculated at 0.25mm in this figure.

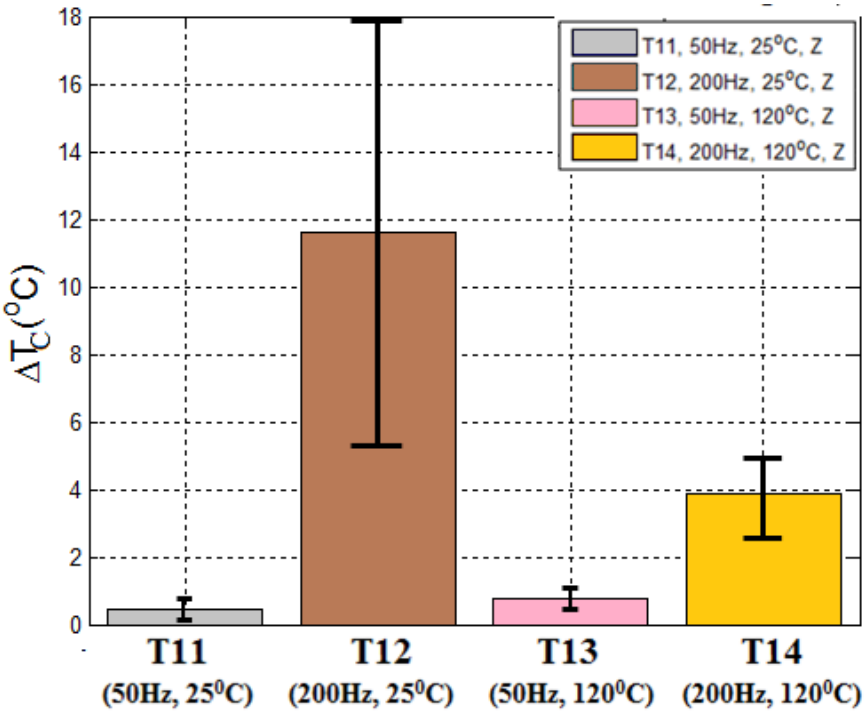

Figure 33: ΔT_C under different vibration frequencies and ambient temperatures (Test 11, 12, 13 and 14)

4.3 Summary and main findings

The accelerated tests have been conducted with various operating conditions including vibration direction, amplitude, frequency and ambient temperature with the measurement R_C and T_C. The measurement data are averaged among three repeating tests.

Generally, the connector degradation and failure are barely observed since there is no significant and gradual increase of R_C during the vibrations. Instead, experiments have shown the temporary increases of R_C during the vibration: When a connector is exposed to vibrations, the R_C significantly increases and oscillates. When the vibrations are stopped, R_C is set back to a value that is close to the original state. The R_C under vibration can increase to a value as large as twice of its original state. This will be analyzed experimentally and theoretically in the following

chapters. The overall increase of connector temperature, ΔT_C, is less significant. It ranges from 0 to 12 degree Celsius based on the operating conditions.

Other findings concerning the effects of different operating conditions include:

- Vibrations at higher amplitudes induce more increase in R_C.
- Vibrations in the X direction (perpendicular to the cable) induce more temporary increase in R_C compared to the Z direction. This can be explained by the analysis in Chapter 6, which shows the vibration in X direction would induce the deformation of the contact spring more directly.
- Vibrations at higher frequency induce more increase in both R_C and T_C. The increase of R_C can be explained by the analysis in Chapter 6, which shows that the relative displacement between the female and male parts tends to follow the increase of vibration frequency. The increase of T_C is likely to be caused by Joule heating with increased R_C. The friction between contact surfaces may be another heat source.
- Vibration at lower ambient temperatures induces more increase in R_C. It is assumed that higher ambient temperatures tend to soften and relax contact material and result in a larger asperity contact area. Therefore, the R_C is smaller at elevated ambient temperatures.

CHAPTER 5 EXPERIMENTAL ANALYSIS OF VIBRATION INDUCED CHANGES IN CONNECTOR RESISTANCE

In the previous chapter, it is found that the connector resistance, R_C, temporarily increased and oscillated during vibration. Experimental works with analysis are conducted in this chapter to explain this experimental finding in this chapter. The analysis will only consider the vibration in the X direction since it induces more increase and oscillation of connector resistance (see Figure 24). The vibrometers are used to measure the motions of connector and the surface profilometer is used to measure the surface profile and roughness for tested connectors.

5.1 Effects of vibration with fixed amplitude and frequency

A vibration test is conducted with a constant amplitude of 0.64mm (peak-to-peak) and a constant frequency of 100Hz. The duration is approximately 37s with 3700 vibration cycles. The ambient temperature is controlled at 25°C and the supplied current is 220A. The test conditions are summarized in Table 5.

Table 5: Test conditions for fixed amplitude and frequency

Amplitude	Frequency	Duration	Current	Ambient Temperature
0.64mm (peak to peak)	100Hz	Approximately 37s	220A DC	25°C

The R_C during the test is shown in Figure 34(a). Again, the temporary increase of R_C is found. When vibration starts, R_C significantly increases and oscillates. When the vibration stops, the R_C decreases to a value that is slightly larger than the original value and remains.

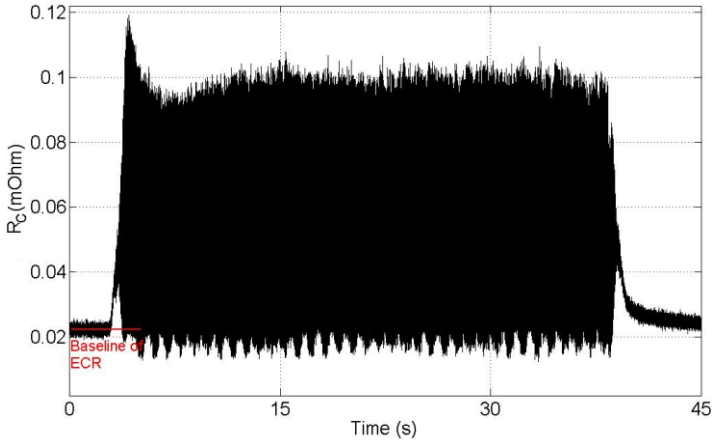

(a) Increase and oscillation of the R_C under 3700 vibration cycles

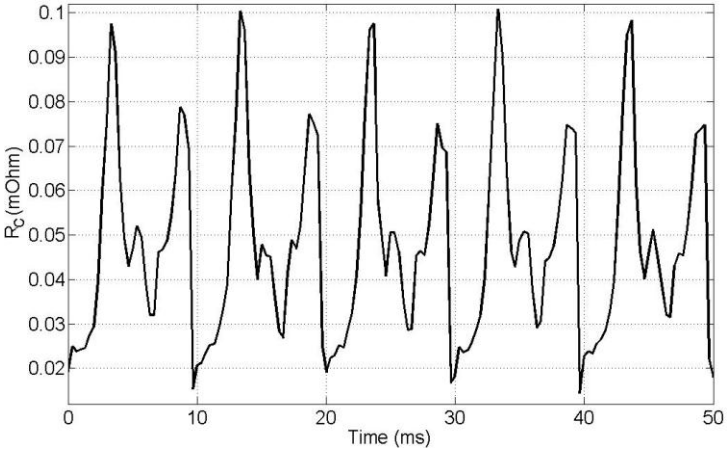

(b) Increase and oscillation of the R_C under 5 vibration cycles

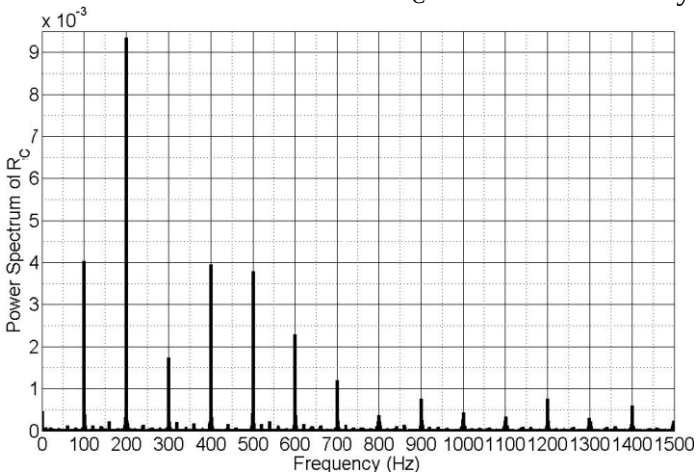

(c) Spectrum of R_C by discrete Fourier transforms

Figure 34: Vibration-induced changes in R_C

Since the data is logged at a high sampling rate, the plot is magnified for a short duration of 50ms, as shown in Figure 34 (b). It is shown that R_C increases and varies periodically, but is distorted from a harmonic signal. The period of the variation has a component at a period of 10ms which is the same as that of the excitation. The spectrum of R_C is analyzed using discrete Fourier transform in Figure 34 (c). It is important to recognize that the spectrum of R_C has the highest magnitude at 200Hz, which is twice as the excitation frequency.

5.2 Effects of vibration with varying amplitudes and fixed frequency

In this test, the vibration frequency is fixed at 100Hz and the ambient temperature is controlled at 25°C. The vibration amplitude is increased from 0.04mm to 0.64mm with an incremental step of 0.04mm at every 30s and then held for 30s without vibration. The measured R_C is shown in Figure 35. It is observed that the R_C tends to follow the increase of the vibration amplitude.

Table 6: Test conditions for varying amplitude and fixed frequency

Amplitude	Frequency	Duration	Current	Ambient Temperature
0.04mm, 0.08mm, …,0.60mm,0.64mm(peak to peak)	100Hz	30s for each amplitude	220A DC	25°C

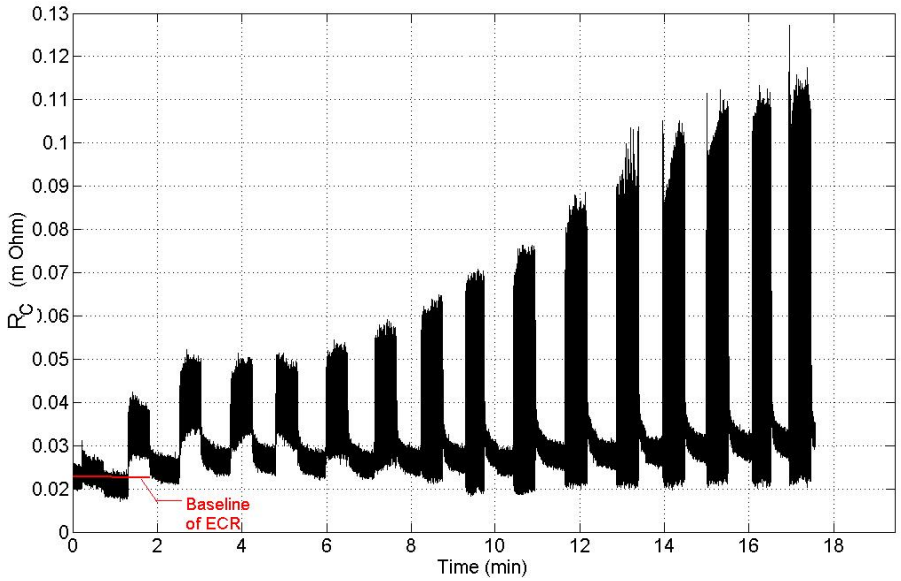

Figure 35 R_C at increasing vibration amplitudes and fixed frequency

The measurement of motions is then applied to this vibration test. In this chapter, the motions at two locations are measured, as shown in Figure 36. U_1 is at the female part of connector and U_2 is at the right end of male part. Two holes are drilled on the female housing and male housing so that the laser beams can measure the two motions. The relative displacement between the right end of male part and the female part is estimated by

$$|U_2 - U_1| = |M_2 \angle \varphi_2 - M_1 \angle \varphi_1| = M_1 \sqrt{\left(1 - \frac{M_2}{M_1}\cos(\varphi_2 - \varphi_1)\right)^2 + \left(\frac{M_2}{M_1}\sin(\varphi_2 - \varphi_1)\right)^2} \qquad (2)$$

where M_1, M_2 and φ_2 are measured from vibrometers. φ_1 equals to zero since U_1 is considered as reference.

Actually, $|U_2\text{-}U_1|$ is an only rough approximation of the relative displacement between male and female parts at the contact surfaces because U_2 is away from the contact surface of male part. The motion at the contact surface of male part, U_4, is not accessible by experiment

because the female part blocks the laser to access it. U_4 can only be calculated by the FEM model, which will be shown in the following chapter.

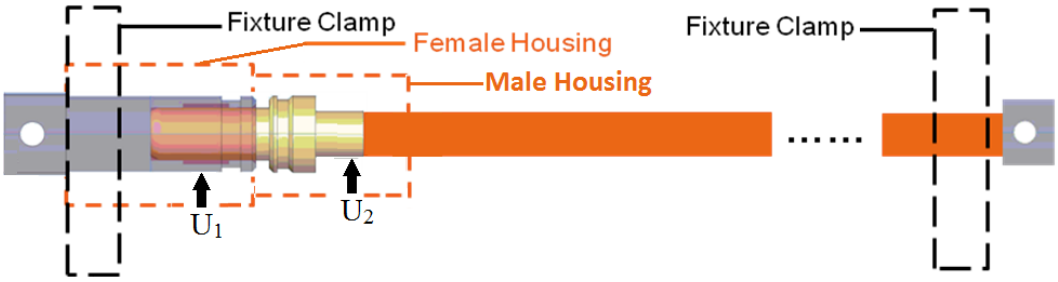

Figure 36: Measurement locations of motions

In order to simplify the presentation of R_C shown in Figure 35, ΔR_C is introduced again as an average value of change of the R_C during vibration. Both $|U_2\text{-}U_1|$ and ΔR_C are plotted as a function of the vibration amplitudes, shown in Figure 37. When the vibration amplitude increases, the relative displacement, $|U_2\text{-}U_1|$, increases. Accordingly, the ΔR_C tends to follow it. This relationship can be approximated by

$$\Delta R_C = k_1 \, | U_2 - U_1 | \tag{3}$$

where k_1 is a constant that can be determined based on the experimental data.

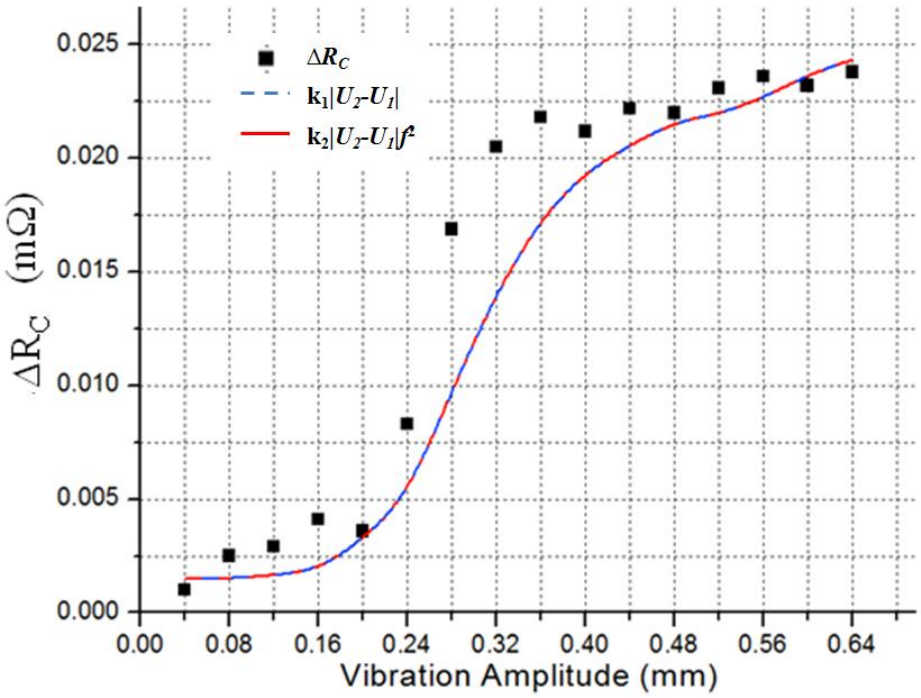

Figure 37: ΔR_C, $k_1|U_2\text{-}U_1|$ and $k_1|U_2\text{-}U_1|f^2$ as a function of vibration amplitude (under increasing vibration amplitudes and fixed frequency)

5.3 Effects of Vibration with Fixed Amplitudes and Varying Frequencies

In this test, the vibration amplitude is constant at 0.15 mm and the vibration frequency is varied from 40Hz to 260Hz with an incremental step of 20Hz every 30s. Other test conditions are unchanged, as shown in Table 7.

Table 7: Test conditions for fixed amplitude and varying frequency

Amplitude	Frequency	Duration	Current	Ambient Temperature
0.15mm (peak to peak)	40Hz, 60Hz, 80Hz, …,240Hz, 260Hz	30s for each amplitude	220A DC	25°C

The relative displacement, $|U_2\text{-}U_1|$, is obtained in the same manner as the previous sections. ΔR_C and $|U_2\text{-}U_1|$ are also plotted as a function of vibration frequency in Figure 38. For

the frequency range that is less than 180Hz, the ΔR_C follows the amplitude of the relative displacement $|U_2\text{-}U_1|$, but it starts to deviate significantly when the frequency is larger than 180Hz. As a result, equation (3) does not represent the ΔR_C over all ranges of the frequency. The ΔR_C should be dependent upon not only the relative displacement $|U_2\text{-}U_1|$, but also the vibration frequency. This relationship can be approximated by

$$\Delta R_C = k_2 \,|U_2 - U_1|\, f^2 \tag{4}$$

as depicted in Figure 38, where k_2 is a constant obtained from experiment data. It shows that the variation of ΔR_C tends to follow the product of relative displacement and the square of frequency, $|U_2\text{-}U_1|f^2$. In the previous section, since the vibration frequency is a constant, equation (4) is also valid and the trend of $|U_2\text{-}U_1|$ and $|U_2\text{-}U_1|f^2$ overlap to each other, shown in Figure 37.

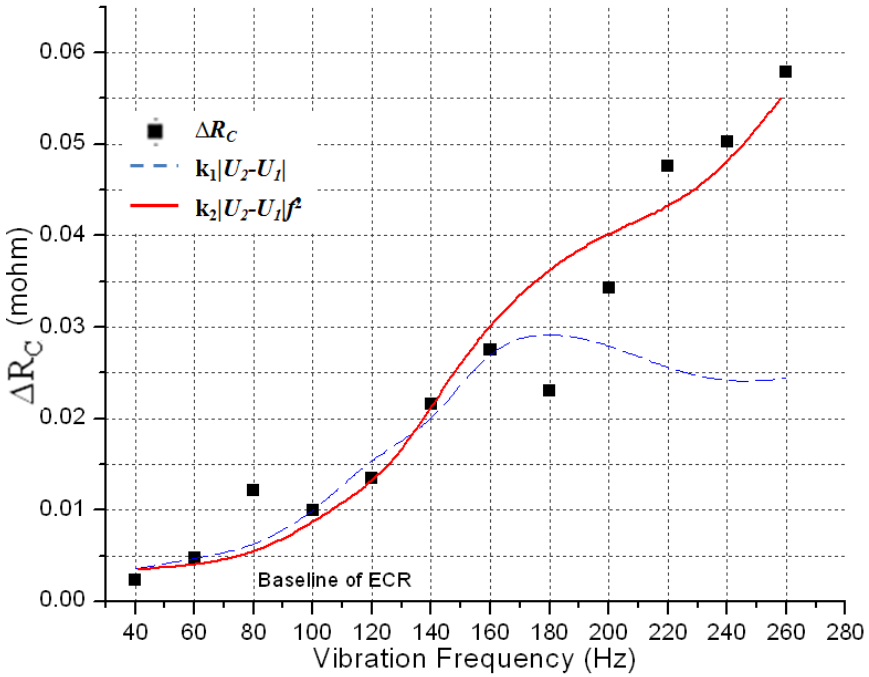

Figure 38: ΔR_C, $k_1|U_2\text{-}U_1|$ and $k_1|U_2\text{-}U_1|f^2$ as a function of vibration frequency (under increasing vibration frequency and fixed amplitude)

5.4 Effects of Vibration with Varying Amplitudes and Frequencies

Like the previous experiments, the ambient temperature is set at 25°C. The vibration frequency is varied from 30Hz to 600Hz with an incremental step of 30Hz, and the corresponding vibration amplitude decreases accordingly under a fixed g-value of 10. Other test conditions are unchanged, as shown in Table 8.

Table 8: Test conditions for varying amplitude and varying frequency

Amplitude	Frequency	Duration	Current	Ambient Temperature
Decreases accordingly under a fixed g-value of 10	30Hz, 60Hz, 90Hz, …570Hz, 600Hz	30s for each amplitude	220A DC	25°C

Based on equation (4), ΔR_C and $k_2|U_2\text{-}U_1|f^2$ are plotted in Figure 39, where k_2 is an experimentally obtained constant. It should be noted that the overall trends of ΔR_C and $|U_2\text{-}U_1|f^2$ are similar. Their peak values are located around the frequency of 150Hz and 450Hz. In addition, $k_1|U_2\text{-}U_1|$ is also plotted in Figure 39 comparison. However, the prediction of equation (3) deviates from the variation of ΔR_C.

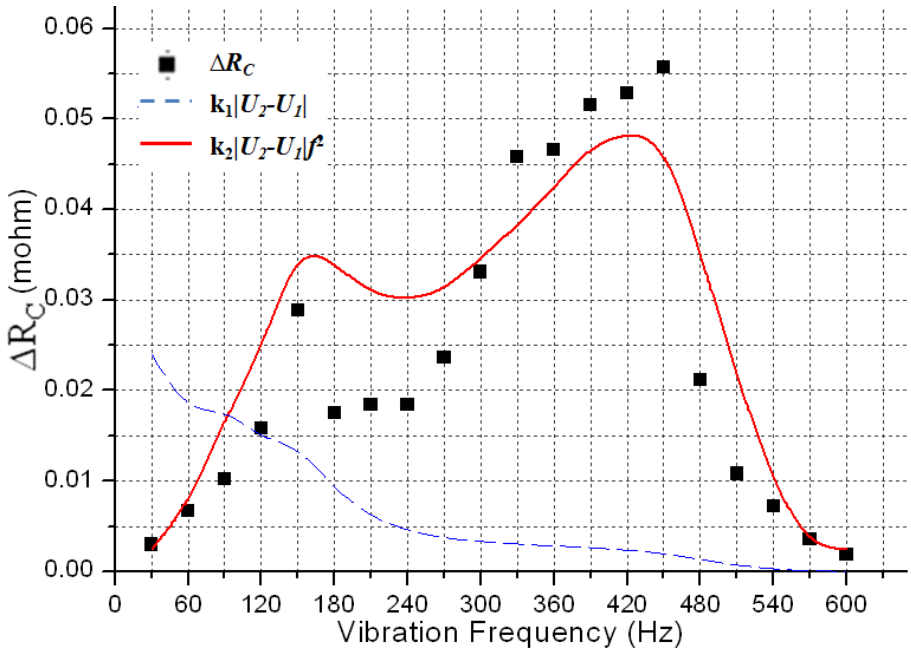

Figure 39: ΔR_C, $k_1|U_2\text{-}U_1|$ and $k_1|U_2\text{-}U_1|f^2$ as a function of vibration frequency (under fixed g-value with increasing frequency and decreasing amplitude)

The results obtained from three experimental cases have shown that the variation of R_C under vibration is affected by both relative displacement between the right end of male part and female part $|U_2\text{-}U_1|$, as well as the vibration frequency. Equation (4) is derived to describe this relationship, where the ΔR_C is based on a product of the relative displacement $|U_2\text{-}U_1|$ and the square of frequency, f^2.

5.5 The effect of vibration on wear and corrosion (Surface analysis)

When vibrations are applied to the connectors, connector resistance changes and wear or corrosion may also occur at the contact surfaces. In order to study the effects of vibration on the surface of the connectors, a vibration with 1mm amplitude and 100Hz frequency is applied to a connector for half an hour, where the ambient temperature during the vibration is set at 80°C. After vibration, the worn connector surfaces are examined and a failure analysis is performed. A

snapshot of a worn surface on the male part of a connector taken from a scanning electron microscopy (SEM) is shown in Figure 40.

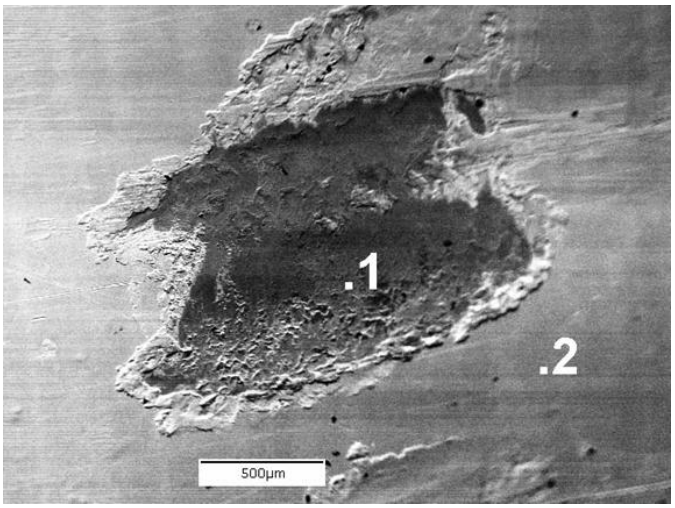

Figure 40: SEM on worn contact surface (Position 1 is wear pit and position 2 is non-contacting area) (From Dr. Michael J. Bozack)

The SEM is operated in backscattered electron mode in order to highlight the different surface morphologies observed on the connectors. Position 1 is the wear pit caused by friction during vibrations. Position 2 refers to the non-contacting area. By observation, the pit in position 1 is just a hole or valley with a lower altitude compared to position 2. Very little material build-up is found.

The results of auger electron spectroscopy (AES) for position 2 and position 1 are shown in Figure 41. AES is a true surface technique, allowing for the detection of all elements of the periodic table (except H) located within the first 50Å of the surface to a sensitivity of ~ 0.01 atom %. In Figure 41 (a), silver is the only element detected in non-worn position. As for Figure

41 (b), copper and its oxide are detected in the worn position where the silver appears to be almost worn out.

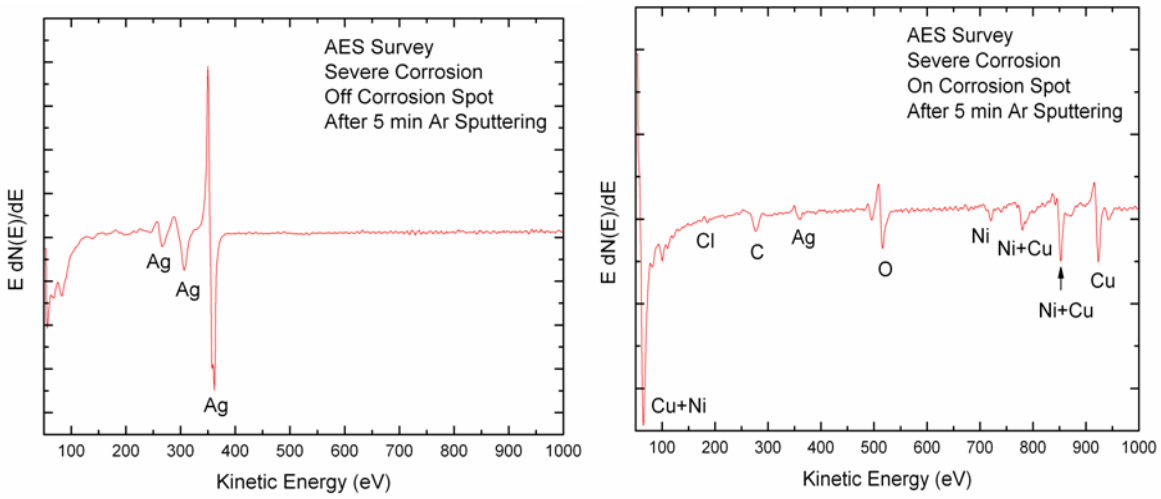

(a) (b)

Figure 41: (a) AES for surface material analysis of non-worn position. (b) AES for surface material analysis of worn position. (From Dr. Michael J. Bozack)

The results show that the defect area on the surface is best referred to as a worn pit rather than corrosion because the main finding is indentation and removal of the coating material. If fretting corrosion occurs, there would be material accumulation and a more random appearance in the SEM image. For example, metallic fretting debris [33] and thick oxide films [14] can be found after tin-plated fretting corrosion.

5.6 Summary

The investigations of R_C and surface analysis have shown that the variation of R_C under vibration is mainly affected by relative displacement and vibration frequency instead of fretting corrosion. It is the relatively stable property of the silver coating that makes fretting corrosion less significant so that the temporary changes of contact resistance dominates the experimental

results. The test results from Hubner-Obenland and J. Minuth also supported the benefits of silver contacts [14]. Their work showed that the silver-to-silver contact has the lowest contact resistance increase after 31 hours of vibration, compared to other combinations of contact materials, including tin, silver, and gold.

CHAPTER 6 MODELING OF THE CONNECTOR SYSTEM USING TWO-DIMENSIONAL FEM

The experimental results obtained in the previous paper showed that the ΔR_C is mainly affected by the relative displacement between the right end of the male part and the female part, $|U_2\text{-}U_1|$. In fact, $|U_2\text{-}U_1|$ is different from the relative displacement between the male (U_4) and the female part (U_1) at the contact surface and the previous analysis was not accurate. In this chapter, we developed a vibration model using FEM to predict U_4, as shown in Figure 42, since U_4 is not accessible for the measurement. As a result, the model allows for accurate analysis on effects of the relative displacement $|U_4\text{-}U_1|$ on the ΔR_C.

As shown in Figure 42, the housing for the male part was removed in this chapter in order to simplify the connector system and make it easier to model. Removing the housing for the male part also helps to study the effects of high natural frequencies that the shaker can excite.

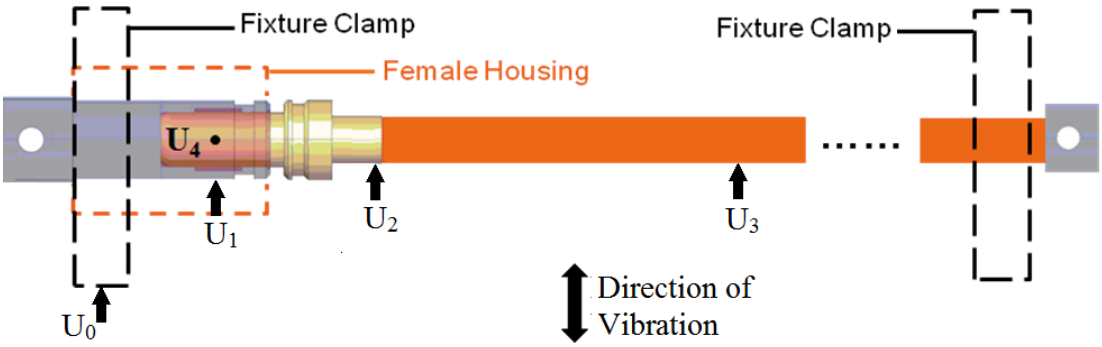

Figure 42: The locations of motions to be studied

6.1 Experimental results

Before showing the FEM vibration model, experiments are conducted to collect the results for validating the model. The test conditions are shown in Table 9. The amplitude of vibrations is set to be with a constant value of 0.18mm, while the frequency is changed from 20Hz to 240Hz with an incremental step of 20Hz. Every vibration lasts 2 minutes at each frequency with a pause of 1 minute. The tests were conducted under flow of constant DC current of 80A and room temperature.

Table 9: Test conditions

Amplitude	Frequency	Duration	Current	Temperature
0.18mm	20Hz, 40Hz, …220Hz, 240Hz	2min for each frequency	80A DC	Room Temperature

The amplitude of the motions, U_0 through U_3, and the connector resistance, R_C, are measured in real time under vibration. Since the connector is fixed with the shaker, it is assumed that U_0 is the same as to the vibration of the shaker. The magnitude ratios of the motions (M_1/M_0, M_2/M_0, *and* M_3/M_0) are plotted in Figure 43.

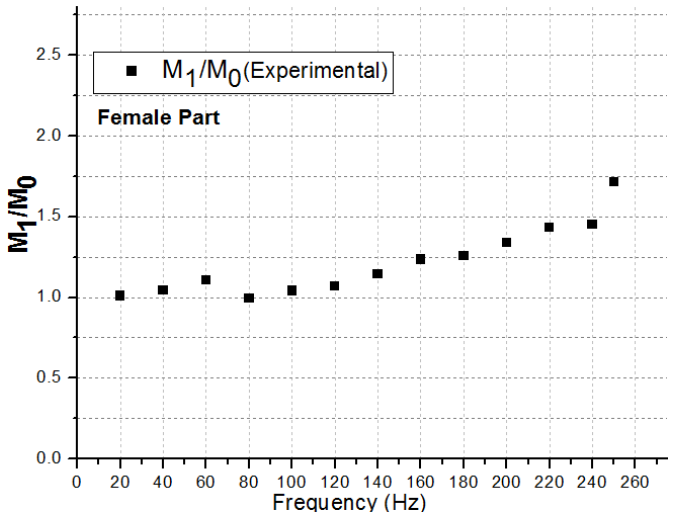

(a) The magnitude of the female part (M_1) versus the excitation (M_0)

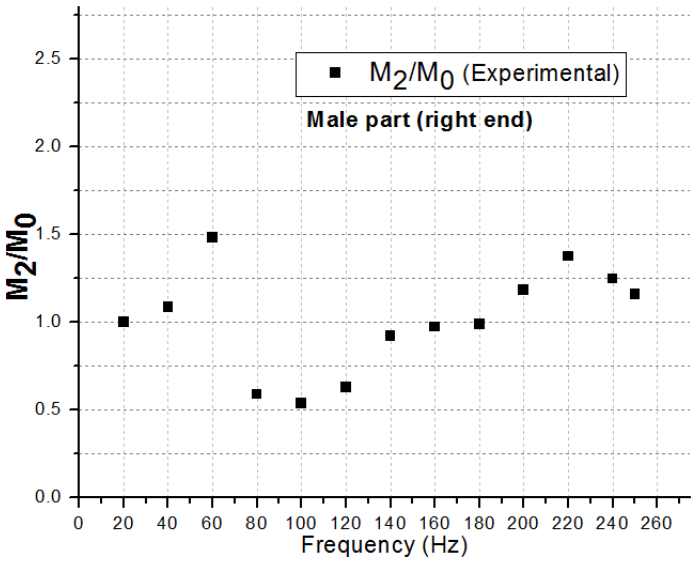

(b) The magnitude of the right end of male part (M_2) versus the excitation (M_0)

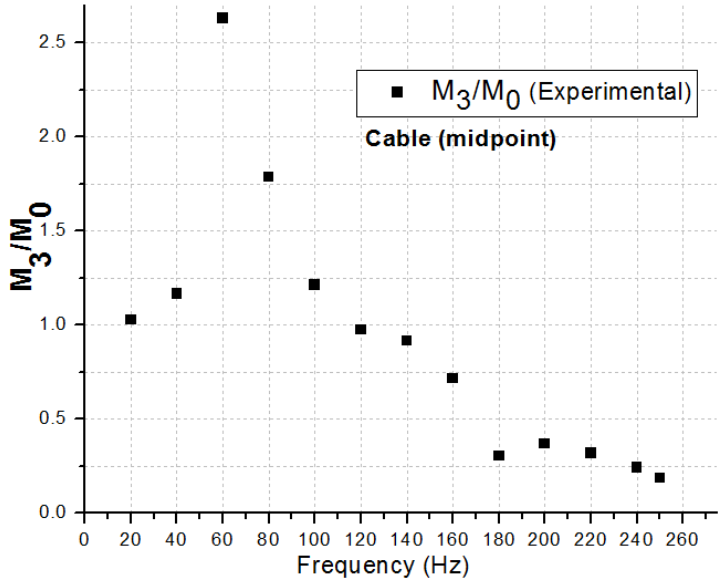

(c) The magnitude of the midpoint of cable (M_3) versus the excitation (M_0)

Figure 43: Experimental results of the magnitude ratios of motions

The frequency response of M_1/M_0 is shown in Figure 43(a), where M_1 is measured at the female part. When the frequency increases, the magnitude increases slightly as well. Figure 43 (b) shows the magnitude of motion at the right end of male part. The magnitude increases significantly at 60Hz and 220Hz, which indicate resonances taking place at the two frequencies. The frequency response of M_3/M_0 is shown in Figure 43 (c), where M_3 is measured at the middle point of power cable. The magnitude increases significantly at 60Hz, which indicates a resonance taking place at the frequency.

Measured ΔR_C as a function of frequencies is shown in Figure 44 . Generally, the connector resistance increases as the frequency increases. The peak values were reached at two resonant frequencies, which will be theoretically verified using the model developed.

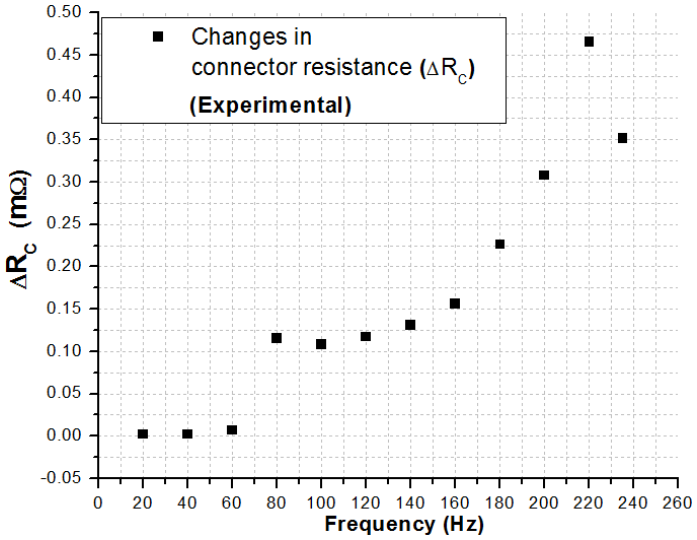

Figure 44: Changes of connector resistance, ΔR_C, versus vibration frequencies.

6.2 Modeling of the Connector System by FEM

6.2.1 Set-up

Set-up for the model is shown in Figure 45(a), where the connector system shown in Figure 42 is simplified to four different components: a female part with housing, a male part, a supplied cable and a contact spring. The female part with housing is regarded as a mass with a shape that encloses the male part and contact spring. The male part and the cable are approximated with two beams that attach to each other, whose material properties and dimensions are shown in Table 10. Since the cable contains copper strands and metal shielding with unknown material properties, the equivalent values are experimentally obtained applying a simple beam theory, where the Young's modules and the density of cable are derived. The contact spring is simplified as two linear springs located between and male and female parts in the direction of vibration.

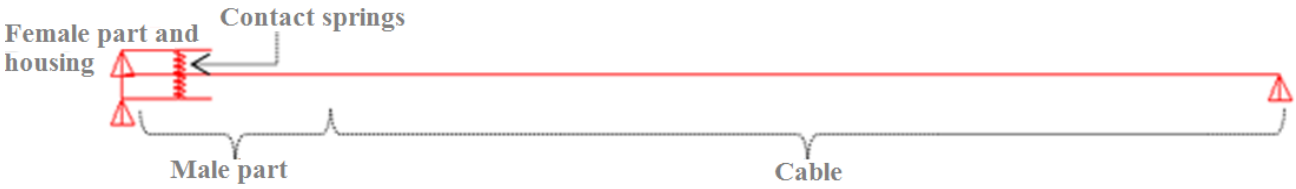

(a) The set-up and boundary conditions in the direction of vibration

(b) The boundary conditions perpendicular to the direction of vibration.

Figure 45: Finite element model for the connector system with boundary conditions.

Table 10: Material and dimensional properties of the male part and cable.

	Connector (copper alloy)	Cable (composite material of strands and shielding)
Young's Modulus (GPa)	117	3.3
Mass Density (kg/m^3)	8930	2506
Length (mm)	60	270
Cross-section area (mm^2)	150	200

Using the commercial finite element software, ANSYS^{TM}, the four simplified components aforementioned are modeled with a two-dimensional structure using one-dimensional elements. All the material properties and the real constants are used for input variables for the element of the Beam3. The contact spring is modeled using the spring-damper element, the Combin14, where a spring constant and a damping ratio are needed. The details of how to determine the spring constant is explained in the following section.

Once the element types with material properties had decided, boundary conditions for the nodes of elements are needed to start simulation. The nodes on the locations of fixture clamps are marked with small triangles and assumed to have the motion same as excitation, as shown in Figure 45(a). Also it is assumed that the displacements of all nodes are in the same direction to

that of the excitation, so no other nodes are vibrating in other directions and corresponding boundary conditions can be set to be zero, as shown in Figure 45(b).

6.2.2 Determination of the equivalent spring constant

The ring shaped spring is approximated with two simple equivalent springs, whose simplification steps are depicted in Figure 46 . The spring has 22 repeatable sections that are uniformly distributed in the circumference and in contact with the female part on one side and male part on the other side. Each section of spring consists of tabs connected over a bridge and is compressed in radial direction by the male part. The 22 repeatable sections are regarded as 22 linear springs that can be reduced to two springs under an assumption that the displacement of the male part is only in the direction of vibration.

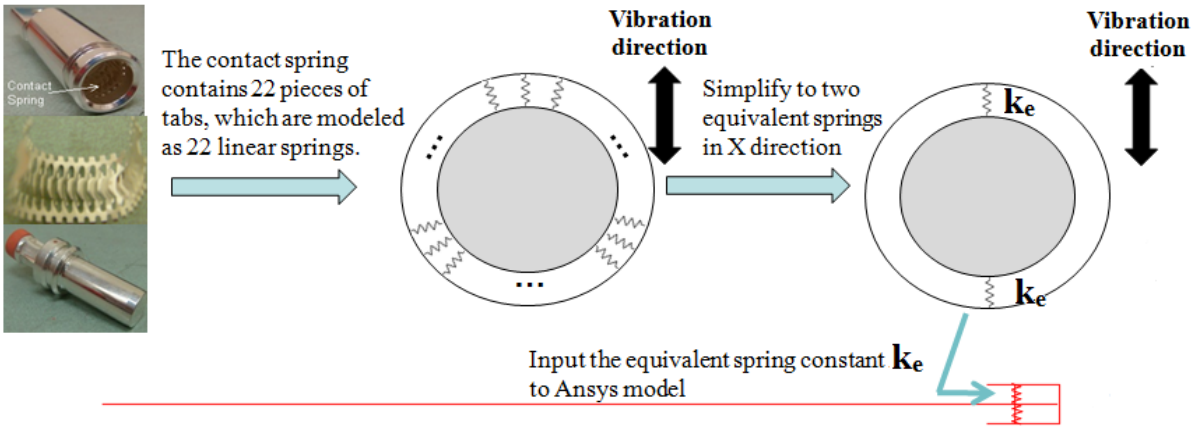

Figure 46: Simplification of the ring shape spring

The spring constant, k_e, is derived from a relationship between force and displacement. The relationship for a single section of the spring is attained from a three-dimensional static simulation and analysis, which will be shown in the next chapter. When the position of male part in the radial direction is artificially and incrementally moved, the corresponding contact force is produced at different positions. As a result, at the i^{th} repeatable section of the contact spring, a

relationship between the radial displacement from a steady state position, r_i (mm), and the radial contact force, $F_{r,i}$ (N), is obtained:

$$F_{r,i} = 24r_i + 8 \tag{5}$$

The linear equation above includes an unknown variable, r_i. When the male part moves in the vibration direction by d, which is known as the relative displacement between male and female part, r_i changes accordingly. As shown in Figure 47 (a), r_i can be expressed as a function of d from the triangle QOP, as shown in equation (6):

$$r_i = d\cos\alpha_i - R + \sqrt{R^2 + d^2(\cos^2\alpha_i - 1)} \tag{6}$$

where R is the radius of male part and α_i is the angle from the x direction to the radial direction of the ith spring.

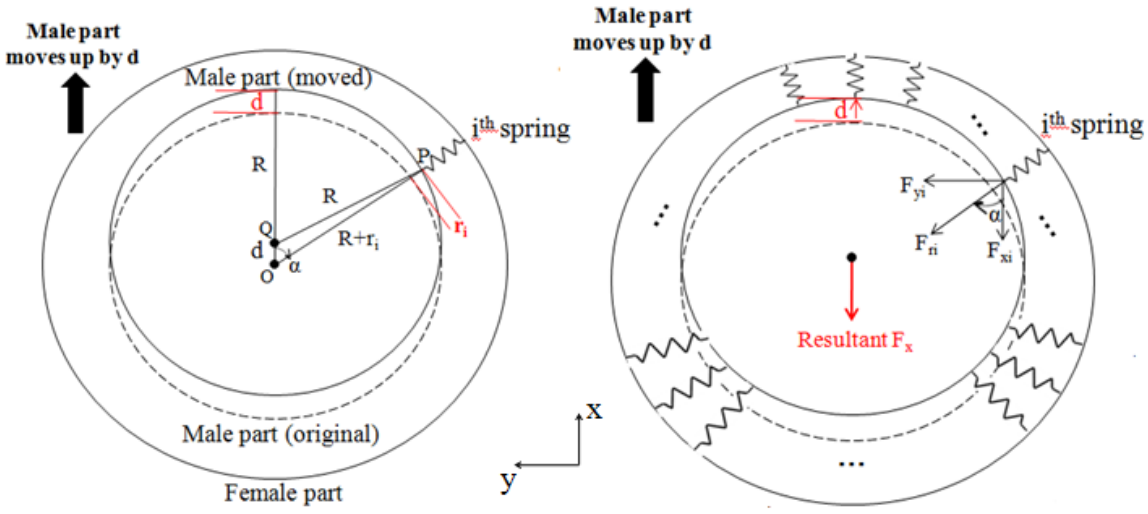

Figure 47: Schematic diagrams for calculation of an equivalent spring constant. (a) Calculation of the radial displacement for the ith spring. (b) Calculation of the resultant force in X direction (direction of vibration)

Hence, the contact force in radial direction for the ith spring is obtained from equation (5) and (6). The force, $F_{r,i}$, can be decomposed into two components, $F_{x,i}$ and $F_{y,i}$, as shown in Figure 47 (b), where the x represents the direction of the vibration. The sum of all forces exerted to y direction is zero because of the cylindrical shape, when the male part is vibrated in x direction. As a result, the resultant contact force, F_x, can be expressed as follows:

$$F_x = \sum_{i=1}^{22} F_{x,i} = \sum_{i=1}^{22} F_{r,i} \cos \alpha_i \tag{7}$$

Consequently, the equivalent spring constant k_e for the two simplified linear springs can be calculated, as shown in equation (8).In this way, the spring constant for the spring element, Combin14, is determined.

$$k_e = \frac{F_x}{2d} = \frac{\sum_{i=1}^{22} \left[24 \left(d \cos \alpha_i - R + \sqrt{R^2 + d^2 (\cos^2 \alpha_i - 1)} \right) + 8 \right] \cos \alpha_i}{2d} = 257 \quad N/mm \tag{8}$$

6.3 Comparison between simulation and experimental results

The vibration model developed above is compared with experimental results obtained using laser vibrometers. The frequency and amplitude of the exciting vibration used for the simulation are same as the experiments, as shown in Table 9, where the marked small triangle in Figure 48 indicates the excited two points in female parts and one point at the end of cable. Like the experimental set-up, U_0, presents a reference point. U_1, U_2, U_3 and U_4 are the points that are calculated in the simulation.

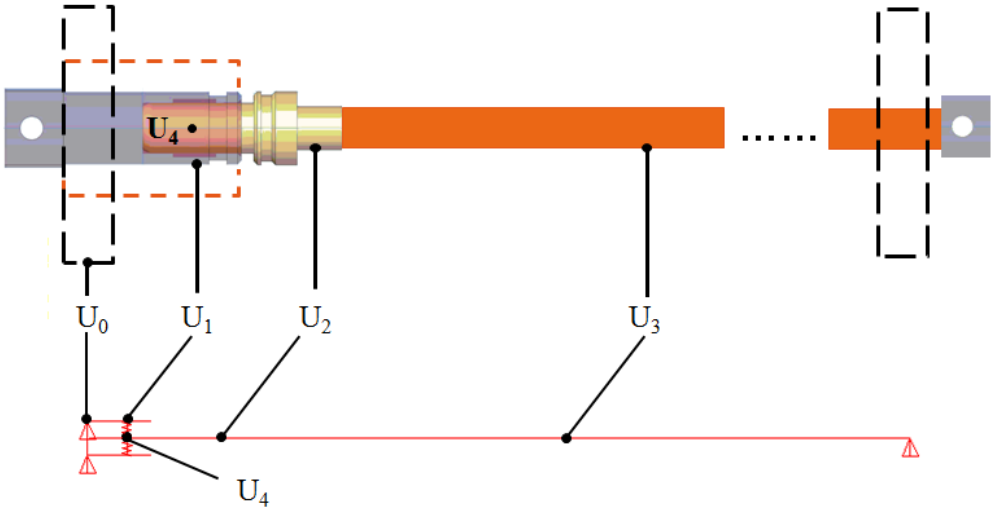

Figure 48: The locations of motions to be studied in simulation

Comparison between simulations and experiments are shown in Figure 49(a), (b) and (c) at different locations, where the magnitude ratios of M_1/M_0~M_3/M_0 are plotted. The results show a fair match to each other in M_1 and M_2, but a deviation around a resonance is observed at M_3.

Because U_4 is inaccessible for a probe, only simulations are carried out and their results are plotted in Figure 50, where the ratio of the magnitude increases at two resonance frequencies of around 60Hz and 190Hz.

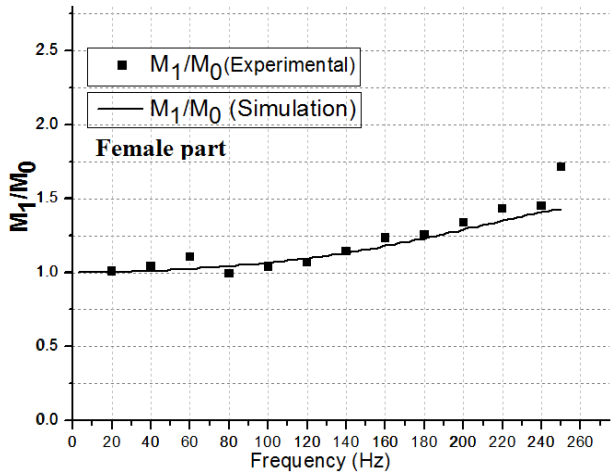

(a) The magnitude of the female part (M_1) versus the excitation (M_0)

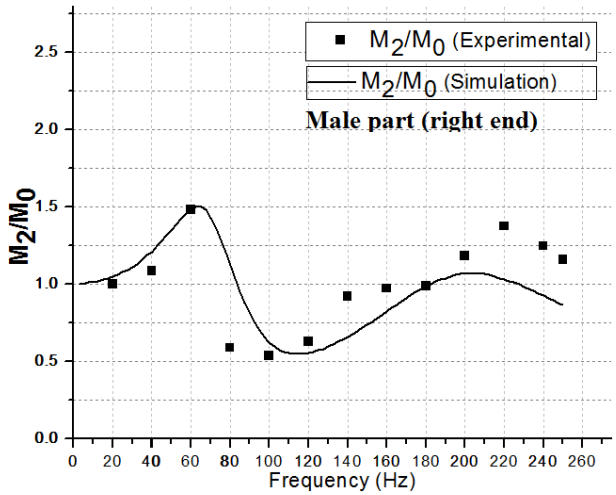

(b) The magnitude of the right end of male part (M_2) versus the excitation (M_0);

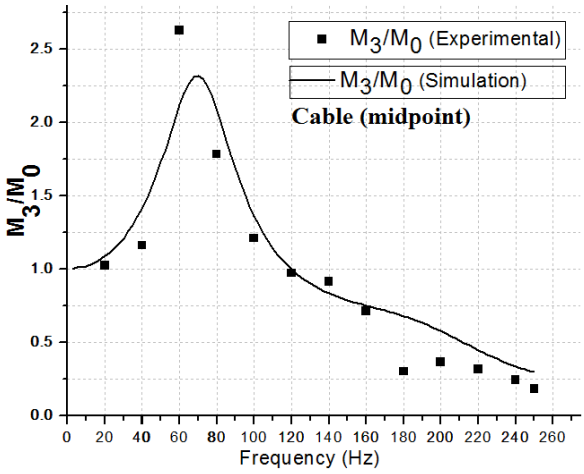

(c) The magnitude of the midpoint of cable (M_3) versus the excitation (M_0)

Figure 49: Comparison between simulated and experimental results

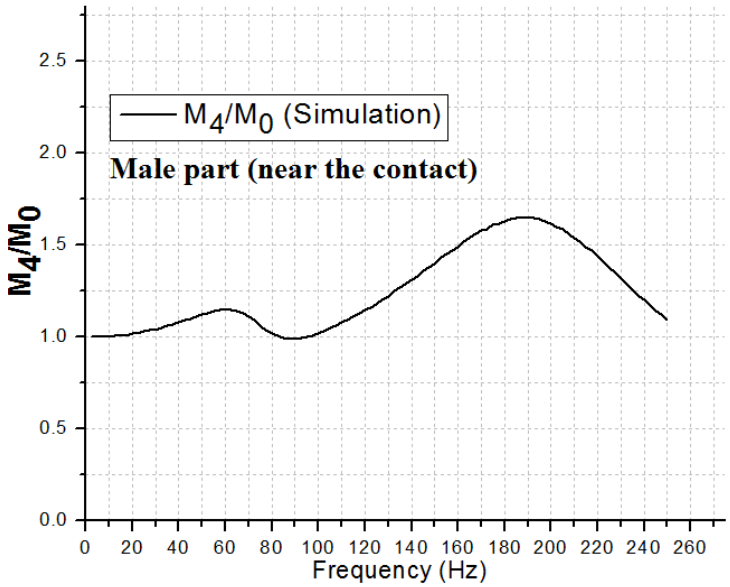

Figure 50: Simulation result: The magnitude of the male part (near the contact) (M_4) versus the excitation (M_0)

Based on the previous results, the relative displacement between the male and female part at the contact surface is studied. The relative displacement, *d*, is defined as an absolute value of the difference between U_4 and U_1, as follows in equation (9):

$$d = |U_4 - U_1| == M_1\sqrt{\left(1-\frac{M_4}{M_1}\cos(\varphi_4-\varphi_1)\right)^2+\left(\frac{M_4}{M_1}\sin(\varphi_4-\varphi_1)\right)^2} \qquad (9)$$

where U_4 and U_1 are calculated using the model .

Simulated relative displacement, *d*, and change of connector resistance experimentally measured, ΔR_C, at different excitation frequencies are plotted in Figure 51. The plot shows a relative good correlation in magnitudes at the two resonant frequencies that are located at the 80Hz and 220 Hz, which implies that the change of connector resistance are affected by the relative displacement at the contact surface.

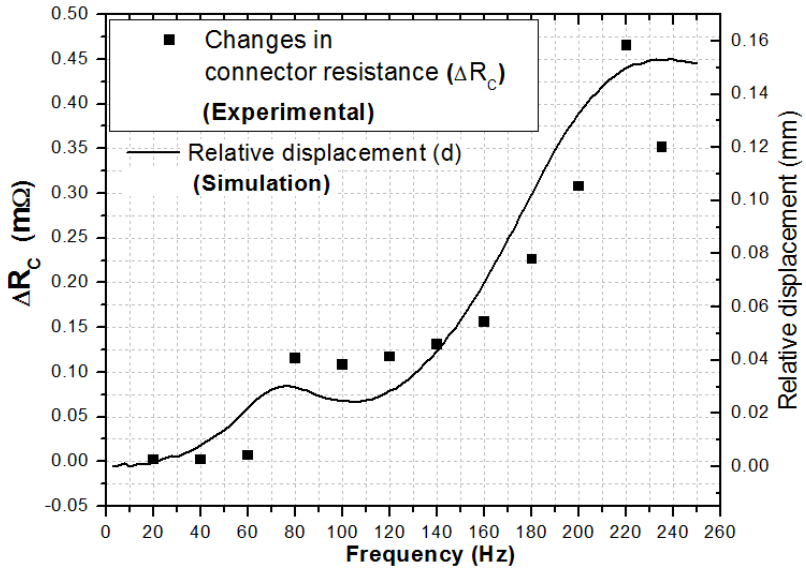

Figure 51: Comparison between relative displacement (simulation) and changes of n connector resistance (experiment)

6.4 Modal analysis by simulation

A modal analysis for the connector system is conducted by simulation. Figure 52 shows the mode shapes of the connector system at the first two natural frequencies. As shown in Figure 52(a), the male part of connector undergoes a rocking motion at the first natural frequency. At the second natural frequency, as shown in Figure 52(b), the male part of connector is more likely to undergo a translational motion in the direction of excitation. These results are similar to the finding from Xie et al. [30], who have investigated the motions of a blade/receptacle connector under vibrations.

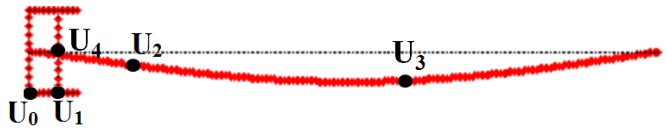

(a) The mode shape at 60Hz, around the first natural frequency

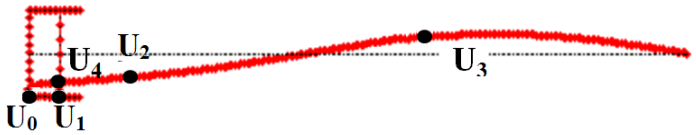

(b) The mode shape at 220Hz, around the second natural frequency

Figure 52: Simulated mode shapes at the first two natural frequencies

The change of mode shape shows that $|U_2\text{-}U_1|$ cannot estimate the relative displacement between male and female parts at the contact surface over all frequency range. As was shown in Figure 38, a deviation is observed between $k_1|U_2\text{-}U_1|$ and ΔR_C at high frequency range because the connector system changed the mode shape when frequency increases beyond a certain value. Equation (4) used the square of excitation frequency, f^2, to compensate this error. However, Figure 51 shows $|U_4\text{-}U_1|$ follows the change of ΔR_C very well over all frequency range, which demonstrates that $|U_4\text{-}U_1|$ is a more straightforward and accurate estimation of the changes of connector resistance compared to $|U_2\text{-}U_1|$.

CHAPTER 7 MODELING OF THE CONTACT SPRING USING THREE-DIMENSIONAL FEM

In order to explain the correlation between $|U_4\text{-}U_1|$ and ΔR_C more clearly, a three-dimensional model for the contact spring is developed using ANSYS™ and used to analyze the time responses of vibrations on displacement of contact surfaces.

7.1 Set-up

Set-up for the model is shown in Figure 53. Since the connector is cylindrical, only a part of the connector along with one section of spring is considered for the modeling. The connector includes one contact surface area of the female and one contact surface area of the male part. According to the actual geometry, the repeatable section of spring has three contact tabs over a bridge, two upper tabs and one lower tab.

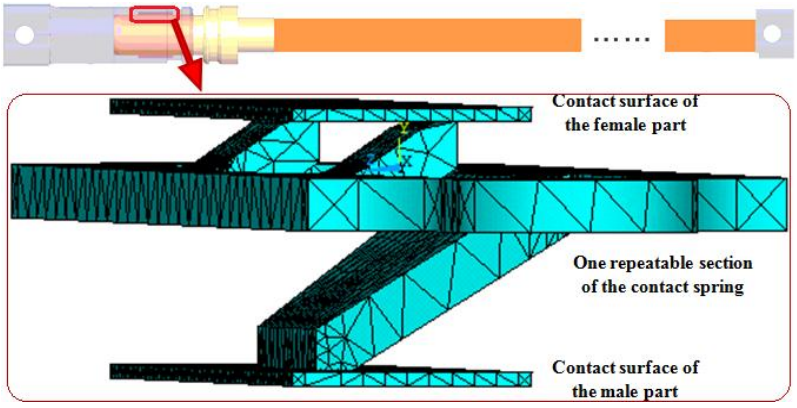

Figure 53: Finite element model of one repeatable section of contact spring.

In order to perform structural analysis of bulk materials, the element of Solid187 is used, which is a high order three-dimensional element with 10 nodes, while Targe170 elements and Conta174 elements are needed for analysis of three contact pairs. The three contact pairs present

two upper tabs and one lower tab. The material properties of the bulk material and the contact pairs are given in Table 1.

Boundary conditions for the spring model are obtained from the simulation results of relative displacements, as shown in Figure 51. When the connector is vibrated, the female and male part oscillates. For simple calculations, the female part is regarded as fixed while the male part oscillates with amplitude of relative displacement, so the boundary conditions for the female and male part are determined. For the spring, symmetric boundary conditions can be applied because of symmetric geometry of only a repeatable section of contact spring modeled. In addition, it is assumed that the displacements of the sides of the spring are only allowed in the direction of vibration.

7.2 Simulation results

The model developed above is used to study time responses of displacements of the spring at four locations: the lower tabs of spring, the upper tab of spring, the contact surface of female part and the contact surface of male part, as shown in Figure 54. Simulations can be run for different cases, so that a case is selected from the data shown in Figure 51, where the relative displacement is 0.153mm at the excitation frequency of 240Hz. The eight periods of the vibration is applied, as shown in Figure 55.

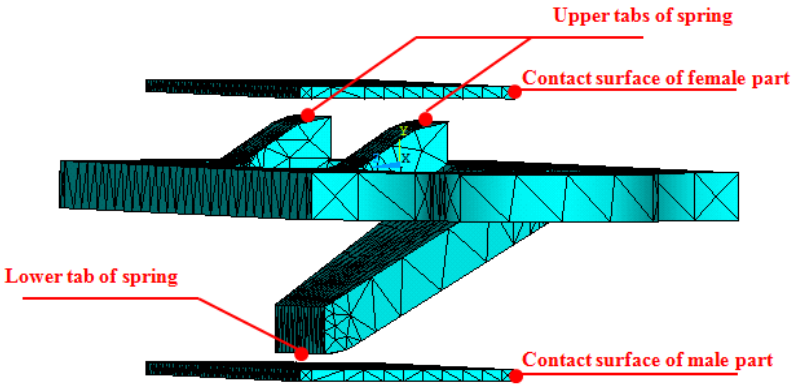

Figure 54: Points for displacement used for simulations

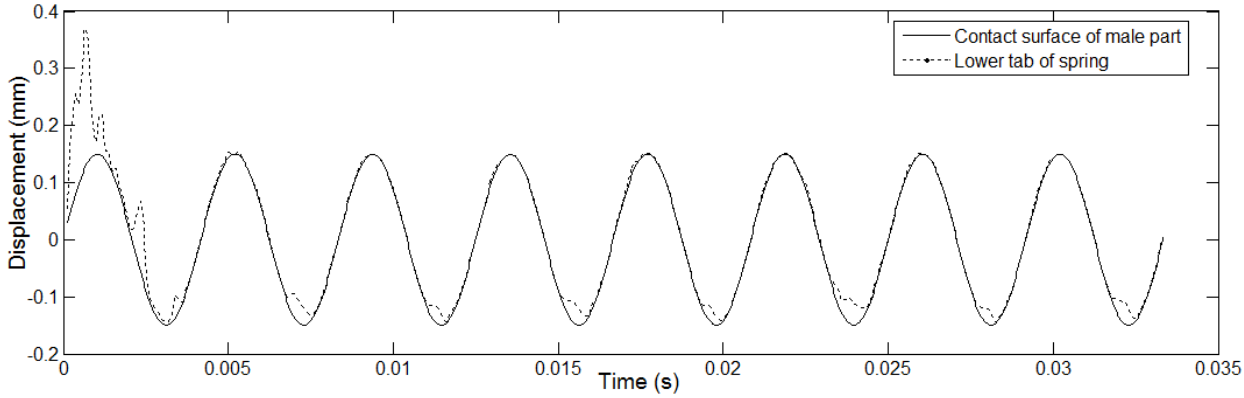

(a) Time response of lower tab of spring

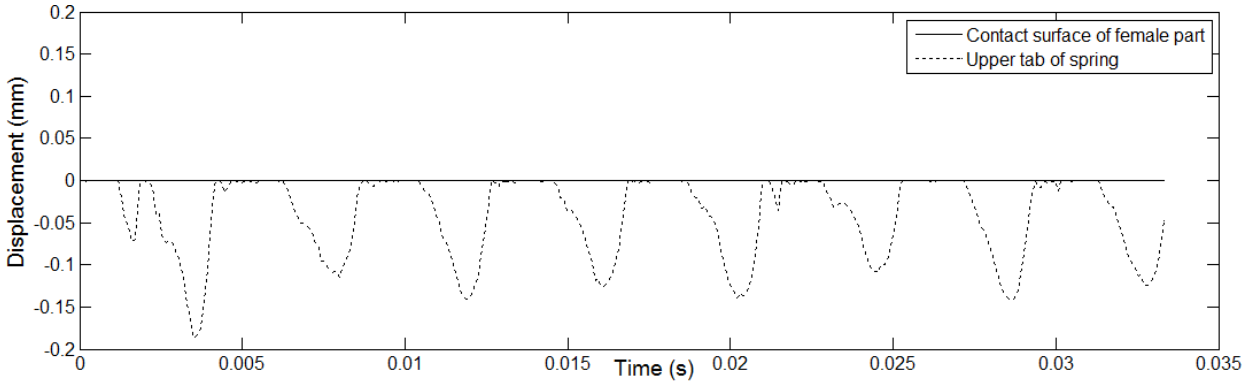

(b) Time response of upper tab of spring

Figure 55: Time response of the displacements versus time when excitation frequency equals to 240Hz

The displacements of lower tab of the spring and the male part are shown in Figure 55 (a), where the displacement of lower tab irregularly varies when vibration is applied and goes into steady state after the second cycle of vibration. In the steady state, overlapped two lines indicate that the lower tab of spring and the male part of connector are in contact. However, contact gaps are formed periodically before the male part reaches maximum and minimum values.

The two upper tabs of the spring are symmetrical from the top view and have the same responses. Therefore, only the responses of one upper tab and the female part are shown in Figure 55(b), where the displacement of the upper tab irregularly varies at the beginning and goes into steady state after the second cycle of vibration. In the steady state, a gap between the upper tabs of the spring and the contact surface of female part is periodically produced, so a contact with the female part is not continuous.

The contact gaps explained above are presented in three-dimensional forms. Three deformed shape of the spring at different instants are shown in Figure 56. When the second cycle starts at t=0.0043s, the shape around the equilibrium position is very little deformed and no contact gap is observed, as shown in Figure 56(a). At t=0.0050s, the male part compresses the spring, so that the low tap loses the contact with the male part, as shown Figure 56(b). At t=0.0070s, the male part releases the spring and the spring loses contact with the female part as well as with male part, as shown in Figure 56(c). The color bar in the Figure 56(d) indicates the displacement of each node in the next contour plots.

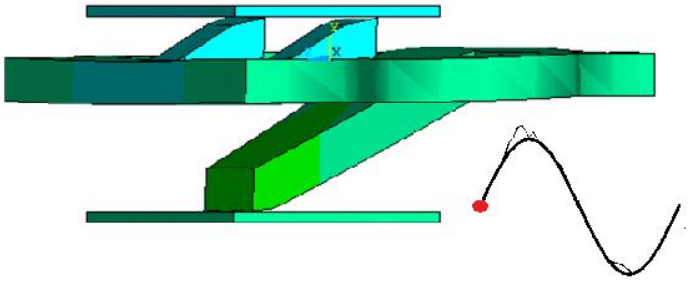

(a) Deformed shape @ t=0.0043s, around equilibrium position

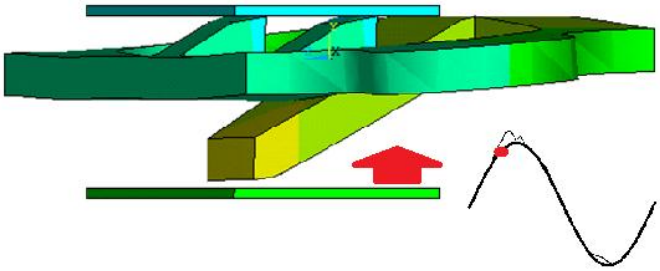

(b) Deformed shape @ t=0.0050s, male part moving up

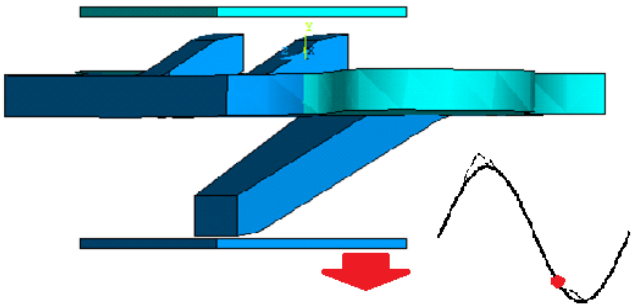

(c) Deformed shape @ t=0.0070s, male part moving down

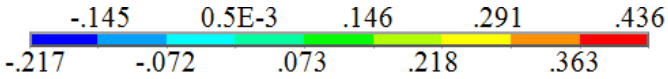

(d) Color bar showing the nodal displacement (mm)

Figure 56: The deformed shapes at different instants, corresponding to Figure 55.

Similarly, studies are performed for two more cases when the excitation frequency is 160Hz and 60Hz and corresponding magnitudes of relative displacements are 0.069mm and 0.022mm respectively, according to the data in Figure 51. Displacements between two contacts are shown in Figure 57, where the second cycle is illustrated. At frequency equaling to160Hz, the gab produced is relatively small, but is negligible at the frequency of 60Hz. The analysis

shows that the gaps between contact surfaces vary when connector is subjected to vibrations. The higher the relative displacement is, the larger the contact gaps are produced, which seemingly cause the changes of connector resistance.

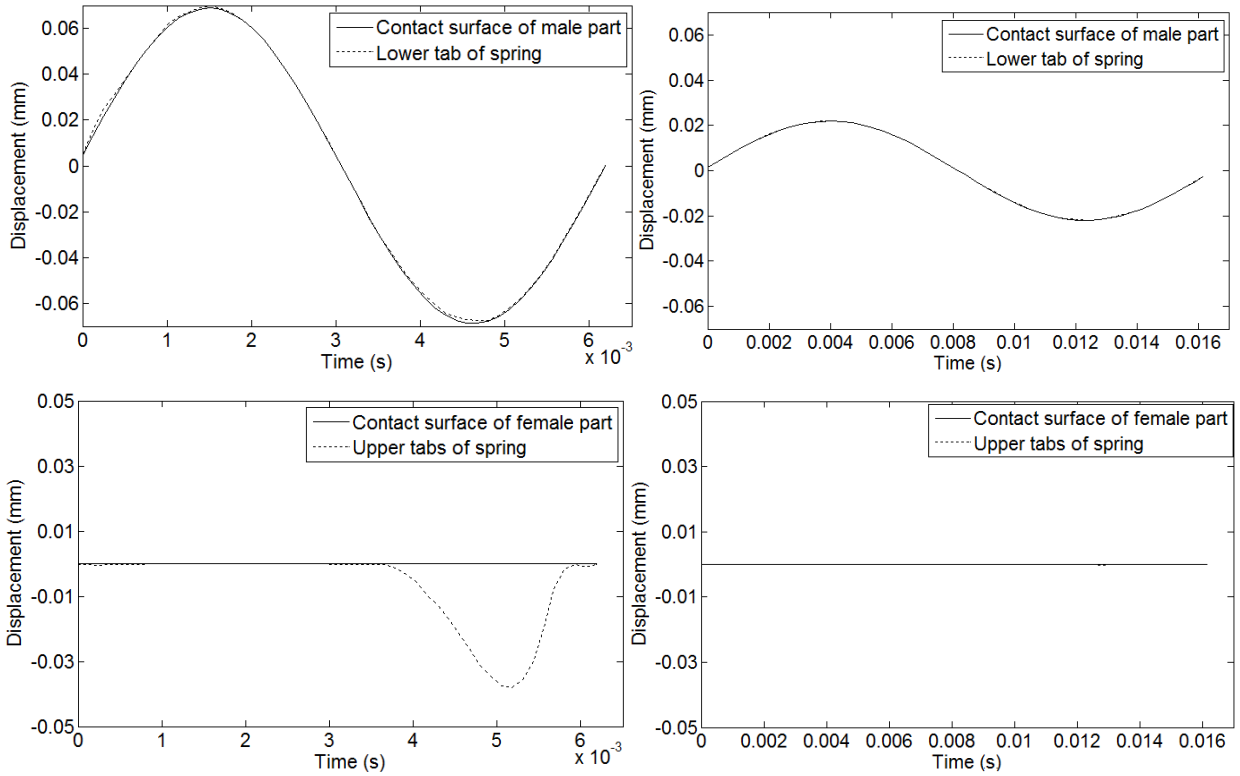

(a)Frequency=160Hz (b) Frequency=60Hz

Figure 57: Time response of the displacements versus time at excitation frequency of 160Hz and 60Hz.

7.3 Comparison of 3D simulation results and experimental data

In order to further study the relation between the changes in connector resistance and the contact gaps under vibration, their spectrums are compared and analyzed using discrete Fourier transform when vibration frequency equals to 100Hz with 0.18mm amplitude. The spectrum of connector resistance measured in experiments is plotted in Figure 58 (a), while the spectrum of

the time response of contact gaps calculated from the three dimensional model is plotted in Figure 58 (b). Figure 58 (a) shows that the spectrum of connector resistance has the magnitude at the excitation frequency (100Hz) as well as its harmonics. The highest magnitude is at 200Hz, which is twice as the excitation frequency. In Figure 58 (b), it is shown that the spectrum of contact gaps has the similar trend as that of the connector resistance. However, the highest frequency locates at 700Hz. This might be caused by the numerical error when the FEM model is converging with oscillations at a frequency around 700Hz.

Finally, the simulations of three dimensional model are conducted at all excitation frequencies in order to compare the changes in connector resistance measured in experiments. As shown in Figure 59, the simulated contact gaps and measured change of connector resistance at different excitation frequencies are plotted in Figure 59. The plot shows that both connector resistance and contact gaps increase when excitation frequency increases. However, the threshold of the increase of connector resistance locates around 80Hz but the threshold of the increase of contact gaps locates around 140Hz. This deviation suggests that the prediction of three dimensional model is not accurate in all frequency domain. This might be caused by neglecting the material yielding and rough surface contact in the three dimensional FEM model.

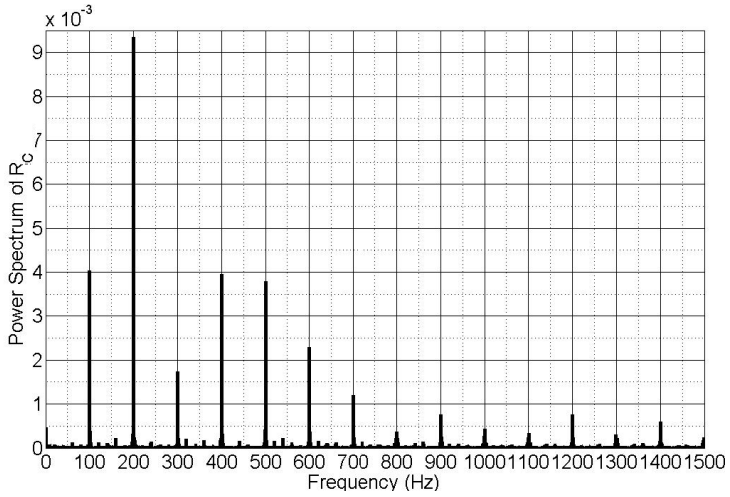

(a) The spectrum of connector resistance (experimental)

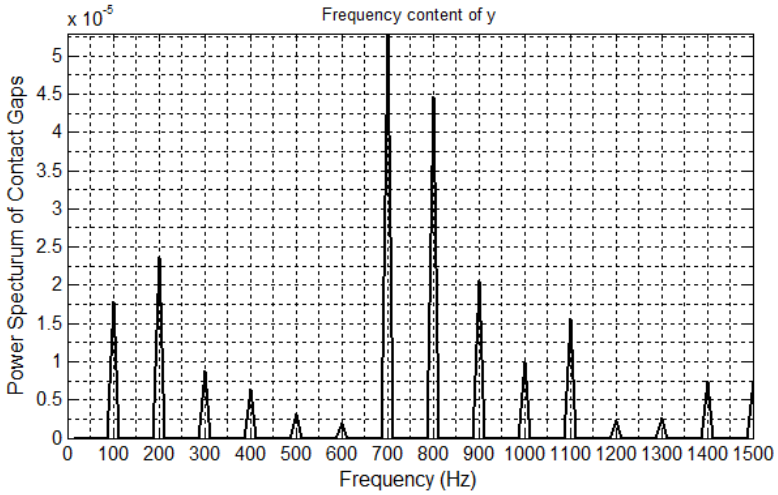

(b) The spectrum of contact gaps (simulation by 3 dimensional model)

Figure 58: The comparison of spectrums of connector resistance and contact gaps under vibrations (excitation amplitude=0.18mm. excitation frequency=100Hz)

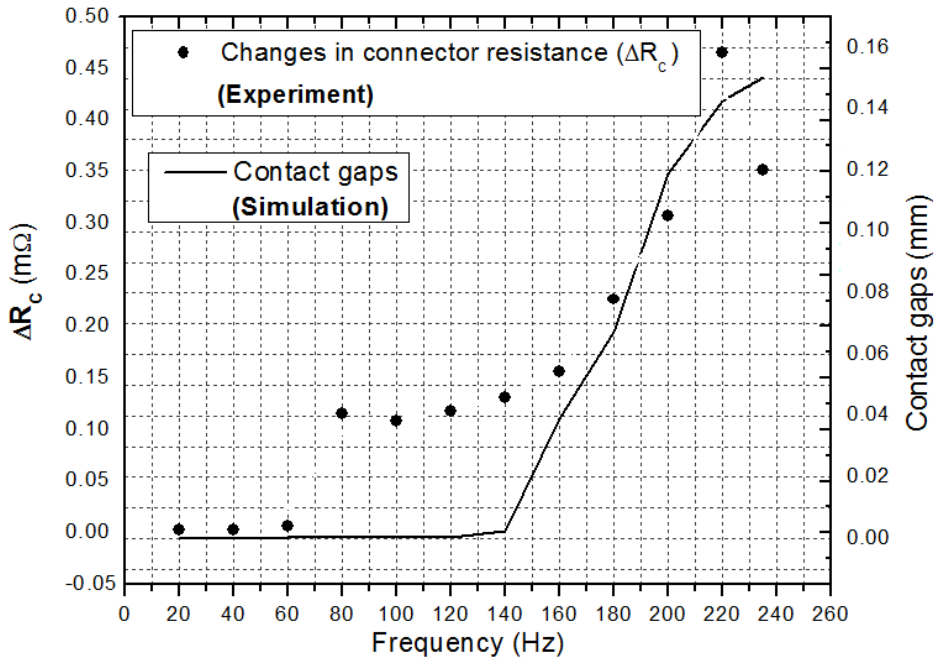

Figure 59: Comparison between contact gaps (simulation) and changes of connector resistance (experiment) in all frequency domains

CHAPTER 8 CONCLUSIONS AND RECOMMENDATIONS

The work presents an experimental and theoretical study on the round pin, silver-plated high power connector used for hybrid vehicles. The temporary change in connector resistance under vibration is found when the tests are conducted under different operational conditions. Theoretical analysis is conducted based on a two-dimensional finite element model for the connector system and a three-dimensional finite element model for the contact spring. The work consists of two parts.

8.1 Experimental findings

A test stand is designed for the connector which facilitates a controlled environment of current supply, vibration and ambient temperature with the measurement of connector resistance, R_C, connector temperature, T_C and motions. In order to study the effects of different operational conditions on the connector, the accelerated tests have been conducted with different vibration directions, amplitudes, frequencies and ambient temperatures. Based on the averaged data among three repeating test iterations, it is found that the temporary increase of connector resistance under vibration, ΔR_C, is more significant under higher vibration amplitude, frequency and lower ambient temperature. Also, vibrations in the X direction (perpendicular to the cable) induce more ΔR_C compared to the Z direction (parallel to the cable).

The temporary increase in R_C under vibration is the most common and significant finding among all test runs: When a connector is exposed to vibrations, the R_C significantly increases and oscillates. When the vibrations are stopped, R_C is set back to a value that is close to the original state. In order to analyze this phenomenon, laser vibrometers are used to measure the motions of

the connector. It is found that the temporary increase in R_C under vibration is affected by the relative displacement between the right end of male part and female part, $|U_2\text{-}U_1|$, as well as the square of vibration frequency.

On the other hand, fretting corrosion of the connector is negligible because R_C does not increase gradually over time under the vibration and has little permanent changes after vibration. Also, according to the surface analysis by SEM and AES on the worn connector, only indentation and removal of the coating material is observed and no accumulation of debris and few oxides are found. It is the relatively stable property of silver that makes fretting corrosion less significant so that the temporary increase of R_C dominates the experimental results.

8.2 Theoretical analysis using FEM

Since the mechanism of the changes in connector resistance under vibration is not clear, a two-dimensional finite element model for the connector system is developed in Ansys™ for analyzing the motions of connector under vibration. The connector system is modeled as simplified components and the contact spring is modeled as linear springs with the equivalent spring constant. The model is simulated and validated by experiments when studying the motions at three locations of the connector system. The model is also able to predict the relative displacement between the male part and female part at the contact surfaces, $|U_4\text{-}U_1|$, which is not accessible for measurement. It is shown that the simulated $|U_4\text{-}U_1|$ tends to follow the measured ΔR_C very well when the excitation frequency is increased. Therefore, the relative displacement at the contact surfaces directly affects changes of connector resistance under vibration. Also, $|U_4\text{-}U_1|$ is a more accurate estimation of ΔR_C than $|U_2\text{-}U_1|$.

However, the spring used for this high power connector has a very complex shape, whose behavior to vibration is unknown. Thus, a three-dimensional model for one repeatable section of the contact spring is developed in Ansys™ to calculate time responses of the spring subject to vibrations. According to the simulation results, the oscillating relative displacement between male and female parts causes the periodic contact gaps between the spring and other connector parts, which changes the connector resistance. According to the time responses, the gaps in steady state are dependent upon the magnitude of relative displacement between the male and female parts.

To sum up, the results gathered in this work have thoroughly explained the mechanism of the vibration-induced changes in connector resistance for the silver-plated, round pin high power connector. When the connector is exposed to vibrations, relative displacement between the male and female parts at the contact surfaces is induced, which in turn causes the periodical contact gaps between contact spring and other parts of the connector. Thus, connector resistance increases and oscillates under vibration.

8.3 Recommendations

The increase of connector resistance during vibration is a potential threat to the reliability of high power connector since it significantly raises the connector temperature due to the high current flow, which is not the case in the low current connector. One suggestion of future work is to investigate the effect of temporary changes in connector resistance on the reliability of connector for high power applications.

In addition, the two finite element models developed in this work are valuable for industry applications to aid in connector design. By investigating the effects of material

properties and geometries, the relative displacement and contact gaps can be reduced and in turn the connector resistance under vibration can be minimized. Therefore, the connector performance and reliability can be improved.

REFERENCES

[1] J. Swingler, J. W. McBride and C. Maul, "Degradation of road tested automotive connectors," *IEEE Trans. Components and Packaging Technologies*, Vol. 23, pp. 157-164, 1999.

[2] C. Maul, J. Swingler and J. W. McBride, "Monitoring the connector environment in automotive systems," *IEEE Seminar on Automotive Electronic Standards*, pp. 5/1-5/4, 1999.

[3] G. Bolger, "The selection of automotive connectors," Senior Thesis, Coventry Univ., U.K., 1997.

[4] J. Swingler and J.W. McBride, "The synergistic relationship of stresses in the automotive connector," in *Proc. 19th Int. Conf. Electrical Contact Phenomena*, pp. 141–145, 1998.

[5] R. B. Waterhouse, *Fretting Corrosion*, Pergamon, Oxford, 1972.

[6] M. Varenberg, I. Etsion and G. Halperin, "Slip index: A new unified approach to fretting," *Tribology Letters*, Vol. 17, pp. 569-573, 2004.

[7] R.D. Malucci, "Stability and contact resistance failure criteria," *IEEE Trans. Components and Packaging Technologies*, Vol. 29, pp. 326-332, 2006.

[8] A. K. Rudolphi and S. Jacobson, "The contact resistance of rolling silver coated copper contacts," in *Proc. 43rd IEEE Holm Conf. Electrical Contacts*, pp. 33-40, 1997.

[9] Y. W. Park, T.S.N.S. Narayannan and K. Y. Lee, "Effect of temperature on the fretting corrosion of tin plated copper alloy contacts," *Wear*, Vol. 262, pp. 320-330, 2007.

[10] J. Swingler, "The automotive connector: The influence of powering and lubricating a fretting contact interface," in *Proc. of the Institution of Mechanical Engineers*, Vol. 214, pp. 615-623, 2000.

[11] G. T. Flowers, F. Xie, M. Bozack and R. Horvath, "Modeling early stage fretting of electrical connectors subjected to random vibration," *IEEE Trans. Components and Packaging Technologies*, Vol. 28, pp. 721-727, 2005.

[12] P. Dijk, A. K. Rudolphi and D. Klaffke, "Investigations on electrical contacts subjected to fretting motion," in *Proc. 21th Conf. Electrical Contacts ICEC*, Zurich, 2002.

[13] G. T. Flowers, F. Xie and M. Bozack, "Vibration thresholds for fretting corrosion in electrical connectors," *IEEE Trans. Components and Packaging Technologies*, Vol. 27, pp. 65-71, 2004.

[14] F. Hubner-Obenland and J. Minuth, "A new test equipment for high dynamic real-time measuring of contact resistances," in *Proc. 45th IEEE Holm Conf. Electrical Contacts*, pp. 193-202, 1999.

[15] Y. W. Park, H. G. Joo and K. Y. Lee, "Effect of intermittent fretting on corrosion behavior in electrical contact," *Wear*, Vol. 268, pp. 353-360, 2010.

[16] E. Carvou and N. B. Jemaa, "Time and level analysis of contact voltage intermittences induced by fretting in power connector," in *Proc. 53rd IEEE Holm Conf. Electrical Contacts*, pp. 211-215, 2007.

[17] D. W. Skinner, "Intermittent opens in electrical contacts caused by mechanically induced contact motion," *IEEE Trans. Parts, Hybrids, and Packaging*, Vol. 11, pp. 72-76, 1975.

[18] J. W. McBride, "Electrical contact bounce in medium-duty contacts," *IEEE Trans. Components, Hybrids, and Manufacturing Technology*, Vol. 12, pp. 82-90, 1989.

[19] E. Carvou and N. B. Jemaa, "Statistical study of voltage fluctuations in power connectors during fretting vibration," *IEEE Trans. Components and Packaging Technologies*, Vol. 32, pp. 268 – 272, 2009.

[20] N. B. Jemaa, "Contacts conduction and switching in DC levels," in *Proc. 48th IEEE Holm Conf. Electrical Contacts*, pp. 1-15, 2002.

[21] J. J. Kopanski, "Intermittent-contact scanning capacitance microscope for lithographic overlay measurement," *Applied Physics Letters*, Vol. 72, pp. 2469-2471, 1998.

[22] S. R. Murrel and S. L. McCarthy, "Intermittence detection in fretting corrosion studies of electrical contacts," *in Proc. 43rd IEEE Holm Conf. Electrical Contacts*, pp. 1-6, 1997.

[23] C. Maul, J. W. McBride and J. Swingler, "Intermittency phenomena in electrical connectors," *IEEE Trans. Components and Packaging Technologies*, Vol. 24, pp. 370-377, 2001.

[24] R. D. Malucci, "Possible mechanism for observed dynamic resistance," *in Proc. 46th IEEE Holm Conf. Electrical Contacts*, pp. 254 - 267, 2000.

[25] C. Maul and J. W. McBride, "A model to describe intermittency phenomena in electrical connectors," in *Proc. 48th IEEE Holm Conf. Electrical Contacts*, pp. 165 - 174, 2002.

[26] W.W. Chen, Q.J. Wang and W. Kim, "Transient thermomechanical analysis of sliding electrical contacts of elastoplastic bodies, thermal softerning, and melting inception," *J. Tribology*, Vol. 131, pp. 021406-1-021406-10, 2009.

[27] N. Saka, M. J. Liou and N. P. Suh, "The role of tribology in electrical contact phenomena," *Wear*, Vol. 100, pp. 77–105, 1984.

[28] J. F. Bruel, P. Smirou and A. Carballeira, "Gas environment effect on the fretting corrosion behavior of contact materials," in *Proc. 14th Int. Conf. Electrical Contacts*, pp. 219-223, 1988.

[29] G. T. Flowers, F. Xie, M. Bozack and X. Hai, "A study of the physical characteristics of vibration-induced fretting corrosion," *IEEE Trans. Components and Packaging Technologies*, Vol. 29, pp. 318-325, 2006.

[30] F. Xie, G. T. Flowers, C. Chen, M. Bozack, J. Suhling, B. I. Rickett, R. D. Malucci and C. Manlapaz, "Analysis and Prediction of Vibration-Induced Fretting Motion in a Blade/Receptacle Connector Pair," *IEEE Trans. Components and Packaging Technologies*, Vol. 32, pp. 585-592, 2009.

[31] C. Chen, G. T. Flowers, M. Bozack and J. Suhling, "Modeling and Analysis of a Connector System for the Prediction of Vibration-induced Fretting Degradation," in *Proc. 55th IEEE Holm Conf. Electrical Contacts*, pp. 131-137, 2009.

[32] G. Zhai, W. Fan and W. Liang, "Study on Contact Resistance Dynamic Characteristics of Space Electromagnetic Relay," *IMACS Multi Conf. Computational Engineering in System Applications*, pp. 1074-1081, 2006.

[33] G. T. Flowers, F. Xie, M. Bozack and R. Horvath, "The influence of contact interface characteristics on vibration-induced fretting degradation," in *Proc. 51st IEEE Holm Conf. Electrical Contacts*, pp. 82-88, 2005.